

An Explainable Neural Radiomic Sequence Model with Spatiotemporal Continuity for Quantifying 4DCT-based Pulmonary Ventilation

Rihui Zhang^{1,2}, Haiming Zhu^{1,2}, Jingtong Zhao³, Lei Zhang^{1,2}, Fang-Fang Yin^{1,2}, Chunhao Wang² and Zhenyu Yang^{1,2}*

¹ Medical Physics Graduate Program, Duke Kunshan University, Kunshan, Jiangsu, China 215316

² Jiangsu Provincial University Key (Construction) Laboratory for Smart Diagnosis and Treatment of Lung Cancer, Duke Kunshan University, Kunshan, Jiangsu, China 215316

³ Department of Radiation Oncology, Duke University, Durham, NC 27710

*Corresponding author:

Zhenyu Yang, Ph.D.

Medical Physics Graduate Program

Duke Kunshan University

Kunshan, Jiangsu, China 215316

E-mail: zy84@duke.edu

Abstract

Accurate evaluation of regional lung ventilation is essential for the management and treatment of lung cancer patients, supporting assessments of pulmonary function, optimization of therapeutic strategies, and monitoring of treatment response. Currently, ventilation scintigraphy using nuclear medicine techniques is widely employed in clinical practice; however, it is often time-consuming, costly, and entails additional radiation exposure. In this study, we propose an explainable neural radiomic sequence model to identify regions of compromised pulmonary ventilation based on four-dimensional computed tomography (4DCT). A cohort of 45 lung cancer patients from the VAMPIRE dataset was analyzed. For each patient, lung volumes were segmented from 4DCT, and voxel-wise radiomic features (56-dimensional) were extracted across the respiratory cycle to capture local intensity and texture dynamics, forming temporal radiomic sequences. Ground truth ventilation defects were delineated voxel-wise using Galligas-PET and DTPA-SPECT. To identify compromised regions, we developed a temporal saliency-enhanced explainable long short-term memory (LSTM) network trained on the radiomic sequences. Temporal saliency maps were generated to highlight key features contributing to the model's predictions. The proposed model demonstrated robust performance, achieving average (range) Dice similarity coefficients of 0.78 (0.74–0.79) for 25 PET cases and 0.78 (0.74–0.82) for 20 SPECT cases. The temporal saliency map explained three key radiomic sequences in ventilation quantification: during lung exhalation, compromised pulmonary function region typically exhibits (1) an increasing trend of intensity and (2) a decreasing trend of homogeneity, in contrast to healthy lung tissue.

1. Introduction

Pulmonary diseases, including chronic obstructive pulmonary disease (COPD), asthma, pulmonary fibrosis, and lung cancer, significantly impact global health, ranking as major contributors to morbidity and mortality worldwide [1-4]. Accurate assessment of lung function is crucial in the clinical management of these conditions [5, 6]. Ventilation, the exchange of air in and out of the lungs, is the most common surrogate of lung function [7-9]. The identification of ventilation defects plays a key role in disease management [10], functional avoidance radiotherapy treatment planning [11, 12] and regional therapeutic response evaluation [4, 13].

Traditional pulmonary ventilation assessments, including forced expiratory volume in one second (FEV_1) [14] and diffusing capacity of the lung for carbon monoxide (DLCO) [15], measure the total volume and flow of air inhaled and exhaled, providing a global view of lung ventilation [16]. These assessments are rapid, easy and commonly utilized in routine ventilation evaluations [17]. However, a key limitation of these assessments is their inability to capture locoregional ventilation conditions in specific lung regions [16]. Consequently, there has been growing interest in advanced imaging techniques that allow for regional ventilation measurement. Positron Emission Tomography (PET) [18] utilizes Galligas for regional ventilation imaging. Galligas is a radioactive aerosol and consists of carbon nanoparticles tagged with the radioactive isotope Ga-68. Administered via inhalation, Galligas emits gamma rays within the lungs, which are detected by PET scanners to produce ventilation images that map the tracer distribution in lung tissues [20]. Single Photon Emission Computed Tomography (SPECT) [19] uses Diethylenetriamine Pentaacetic Acid (DTPA) radiolabeled with Technetium-99m for regional ventilation imaging. Administered as an aerosol through inhalation, DTPA disperses within the lungs and emits gamma rays, which are detected by SPECT scanners to produce ventilation images [20, 21]. Additionally, Hyperpolarized Noble Gas (HNG) Magnetic Resonance Imaging (MRI) has been explored as another approach for regional ventilation imaging [22]. Patients inhale the HNG, such as helium-3 [23] or xenon-129 [24], and the hyperpolarization of the gas enhances the nuclear magnetic resonance (NMR) signals, allowing precise imaging of gas distribution within the lungs [25, 26]. Similarly, Xenon-Enhanced Computed Tomography (CT) has been investigated in feasibility studies [27], with xenon gas improving contrast in CT scans and enabling clear delineation of pulmonary gas distribution due to its high density and atomic number. Despite the utility of these methods, they come with limitations, including the need for specialized tracer gases and equipment, high costs, lengthy procedures, and potential radiation exposure to patients [12, 28].

In recent years, significant progress has been made in the development of advanced ventilation imaging techniques capable of identifying ventilation defects [29]. Among these, the four-dimensional CT (4DCT)-based Computed Tomography Ventilation Imaging (CTVI) techniques have emerged as promising tool [10, 12]. Unlike traditional CT scans that provide static anatomical insights, 4DCT captures dynamic information by recording lung deformation throughout the tidal breathing cycle [30]. CTVI techniques analyze lung motion in 4DCT scans by registering lung regions across various respiratory phases using deformable image registration (DIR) [31-33]. This process generates displacement vector fields (DVF), where each vector represents the displacement of individual voxels between respiratory phases [9, 10, 32]. Local volume changes at each voxel can be quantified using the Jacobian Determinant of the DVF (DIR-JAC method) or variations in CT Hounsfield Units between registered voxels (DIR-HU method), with areas of significant volume change indicating higher ventilation activity [9, 31]. The efficacy of CTVI relies heavily on the accuracy of the DIR algorithm and the precision of lung motion modeling [10, 34-37]. Despite advancements in CTVI accuracy, standardized implementation workflows have yet to be established, and achieving robust and reproducible CTVI results across diverse patient populations and clinical settings remains a challenge [9, 10, 37]. Driven by rapid developments in algorithms and computational power, the integration of radiomics with machine learning has emerged as a novel, DIR-independent approach for lung ventilation estimation [38]. Radiomics involves extracting quantitative intensity and texture features that are defined based on experts' domain knowledge from lung imaging [39, 40]. These features are treated as potential biomarkers that reflect the underlying physiological and pathological states of the lung image [41, 42]. Machine learning algorithms can be trained to associate these features with various pulmonary conditions and lung function metrics [36, 43]. Previous radiomic studies have demonstrated correlations between features extracted from whole-lung CT images and global ventilation measurements such as FEV₁ and DLCO [44]. Our pilot studies extended this approach by employing voxel-based radiomic extraction, also known as radiomic filtering, to derive spatially encoded intensity and texture features within specific lung sub-regions [45]. Preliminary results suggest that radiomic-filtered feature maps derived from average 4DCT lung volumes may correlate with regional pulmonary ventilation [45]. Moreover, advanced machine learning techniques, such as deep neural networks (DNN), have also been investigated for ventilation quantification. DNNs utilize multilayered neural networks to progressively learn lung CT or 4DCT image features in a supervised manner, directly predicting lung ventilation distributions. Studies indicate that DNN-based approaches have improved ventilation quantification accuracy while eliminating the dependence on DIR [43]. Despite these advances, radiomics and deep learning-based methods do not

fully account for the dynamic nature of continuous lung motion and deformation. Additionally, a notable limitation of existing radiomic models is their lack of explainability. Machine learning models, particularly DNN-based analyses, process large datasets in a nonlinear and nested fashion to reach probabilistic decisions [47], making it difficult to interpret the key image features and respiratory motion parameters contributing to ventilation quantification [46]. As a result, these models remain “black boxes” in their implementation [47].

In this study, we aim to develop an explainable neural radiomic sequence model that incorporates spatiotemporal continuity for identifying regions of compromised pulmonary ventilation function using 4DCT images. The locoregional lung intensity and texture were first extracted from the 4DCT data as a function of the respiratory cycle, thereby generating a temporal sequence of radiomic features, referred to as radiomic sequences. Long short-term memory (LSTM), a type of deep neural network (DNN) model known for its efficiency in processing temporal information [50, 51], was employed in this study. Specifically, we developed an explainable LSTM model to associate voxel-wise spatiotemporal radiomic sequences with measured ventilation defects, as validated by DTPA-SPECT and Galligas PET. To explain the contribution of individual radiomic sequences and respiratory phases in quantifying ventilation defects, we derived a specially designed temporal saliency map. This map highlights the key radiomic sequences and critical time steps (i.e., respiratory phases) involved in the quantification process. To the best of our knowledge, this work is the first to incorporate spatiotemporal lung dynamics into a radiomics-based model. Our methodology not only achieves high accuracy in lung ventilation defect quantification but also enhances the interpretability of the model’s outputs. Given the widespread clinical use and acceptance of 4DCT [34, 52], this positions our proposed methodology as a potential complementary tool to existing pulmonary quantification techniques.

The main contributions of our work can be summarized as follows:

- Our radiomic sequence modeling extends traditional radiomic analysis from static image to time-dependent 4DCT: by implementing the radiomic filtering throughout the entire 4DCT scan, the locoregional lung texture and intensity heterogeneities can be modeled as spatiotemporally continuous sequences. To our knowledge, this is the first application of a model that captures motion-induced changes in radiomic features as time-dependent sequences.
- We introduced a novel explainable neural radiomic sequence model that utilized radiomic sequence with spatiotemporal continuity to accurately identify compromised pulmonary ventilation regions. Our model identified regions of lung defect with an average Dice coefficient of 0.78/0.78 compared to the PET/SPECT images, and an average voxel-wise Receiver Operating

Characteristic Area Under the Curve (AUCROC) of 0.85/0.84. These results significantly outperform other deep learning-based methods for lung ventilation quantification.

- The explainable LSTM model innovatively generates temporal saliency maps, which identify key radiomic sequences and critical time steps (i.e., respiratory phases) that are essential for accurate ventilation quantification. In these saliency maps, the horizontal axis represents the feature sequence, while the vertical axis represents the time steps. Each coordinate point on the map indicates the importance of the corresponding feature sequence at a given time step. Brighter areas on the map correspond to higher importance, allowing for a direct and interpretable understanding of the predictive mechanisms driving the model.
- Given the broad clinical adoption of 4DCT, our proposed method holds potential for generalization to other respiratory-related image analyses.

2. Related work

This section conducts a literature review for CTVI, radiomics/deep learning-based ventilation imaging, time series modelling, and the explainability of time series models.

2.1. *Computed tomography ventilation imaging*

Currently, the CTVI technique is primarily based on two different approaches: the DIR-JAC and DIR-HU methods. Both methods begin by applying direct image registration (DIR) between the exhale and inhale phase images of 4DCT to generate the DVF [10]. The DVF describes how each voxel in the exhale image maps to the corresponding voxel in the inhale image. The DIR-JAC method utilizes the Jacobian determinant of the DVF to measure regional volume changes. Specifically, the Jacobian determinant is derived from the spatial gradients of the DVF and represented as a matrix of partial derivatives. This determinant quantifies the scaling factor of the transformation at each voxel and can be interpreted as regional volume change. Determinant values greater than 1 indicate expansion and values less than 1 indicate compression. Ventilation estimations at the voxel level are then calculated based on these regional volume changes, where regions with significant expansion reflect higher ventilation activity [9, 43]. On the other hand, the DIR-HU method interprets changes in HUs between registered voxels as indicators of regional volume changes [9, 48]. Specifically, the change in HU values is converted into a quantitative measure of volume changes, where a larger decrease in HU corresponds to greater local expansion. Ventilation estimations at the voxel level are then derived based on these regional volume changes. Castillo, Castillo [49] conducted a comparative analysis between the DIR-JAC method and the DIR-HU method, determining that both approaches exhibited comparable performance. Hegi-Johnson, Keall [50] also evaluated the accuracy of different CTVI methods (i.e., DIR- JAC method and DIR-HU method) by comparing them with Technegas SPECT and found that 4DCT image quality may significantly impact on CTVI accuracy. The VAMPIRE Challenge [9] evaluated 37 distinct CTVI algorithms using the VAMPIRE dataset based on the Spearman coefficient. The results revealed significant variability in algorithm performance, which may be largely attributed to differences in DIR methods. Hegi-Johnson, De Ruyscher [10] systematically reviewed the literatures for CTVI and emphasized that a key challenge in CTVI lies in its heavy reliance on the accuracy of DIR algorithms and the precision of lung motion modeling.

2.2. Radiomics/Deep Learning-based ventilation imaging

With advancements in computational power, image quantification techniques such as radiomics and deep learning have been applied to identify patterns from images that are associated with underlying physiological and pathological conditions. Typically, radiomics first determines the volume-of-interest (VOI), e.g., lung in ventilation estimation tasks, and extracts the radiomic features that are defined based on experts' domain knowledge to quantitatively capture the intensity, shape, size or volume, and texture information of VOIs [51, 52]. The extracted features can be considered as the potential biomarkers that reflect patient underlying pathophysiology and can be associated with the lung ventilation [38, 44, 45]. Lafata, Zhou [44] has identified a correlation between the radiomic features extracted from entire lungs on CT images with global ventilation measurements (i.e., FEV₁ and DLCO). Yang, Lafata [45] extracted spatial-encoded radiomic intensity and texture features within each sub-region of the averaged lung 4DCT and further demonstrated that these locoregional radiomic features could correlate with the regional pulmonary ventilation. Westcott, Capaldi [38] extracted locoregional texture radiomic features from lung three-dimensional CT (3DCT) and employed support vector machine to produce regional ventilation estimations in COPD patients. Deep learning is an emerging approach for image quantification and characterization [53]. Deep learning networks, which consist of multi-layer feed-forward neural networks, can be trained end-to-end in a supervised manner using medical images paired with measured ventilation imaging data [54]. Through hierarchical progressive operations on the images, deep learning networks learn the high-level abstractions that capture the intrinsic representation of the image linking the input image to the outcome [55]. Convolutional neural networks (CNNs) are widely used deep learning architectures in medical imaging [52], with U-Net being one of the most popular examples [56]. Zhong, Vinogradskiy [54] introduced a convolutional neural network (CNN) model for deriving ventilation images from 4DCT scans. Liu, Miao [43] developed a U-Net CNN model to produce ventilation images from 4DCT scans, offering the first comparison with CTVI and greatly improved accuracy in comparison to DIR-HU and DIR-JAC methods. Kajikawa, Kadoya [57] proposed a U-Net CNN model for translating CT to SPECT ventilation imaging and quantifying the model uncertainty. However, the performance of these radiomics/deep learning-based analyses still can be improved. Another issue is that they haven't fully explored the continuous lung motion and deformation information from the 4DCT. The deep learning networks also lack explainability; their use of non-linear and complex processes to handle data makes them difficult to explain in a straightforward manner to humans [58].

2.3. *Times series modelling*

Time series data is a collection of observations recorded sequentially in chronological order [59, 60], which can be categorized into univariate and multivariate time series. Typically, univariate time series data represents a single variable measured over multiple time steps [61], while multivariate time series data involves multiple variables measured simultaneously over time steps [62]. Time series data is typically treated as a unified whole rather than as separate numerical fields due to its high-dimensional and continuous nature [60]. Analysis of time series data mainly focuses on capturing its temporal dependencies including short-term and long-term dependencies [63]. Various deep learning algorithms have been developed to analyze such data, including recurrent neural networks (RNNs), long short-term memory networks (LSTMs), bi-directional LSTMs (BiLSTMs), and Transformers. RNNs are subset of DNN [64] and includes various types such as fully RNN [65-67] and selective RNN [68]. The typical feature of RNNs is their cyclic connections, which enable these networks to update their current state by integrating information from past states and current input data [64]. RNNs have proven their efficacy in processing temporal information inherent in time series data [64, 69, 70]. The previous studies have demonstrated that the traditional RNN model can be limited by vanishing or exploding gradient problems during the training [69]. Another limitation of RNN model is the inefficacy in capturing the long-term dependencies, especially when processing long sequence data [69]. The LSTM architecture was subsequently proposed based on the RNN [71]. LSTMs consist of an internal memory and multiplicative gates that regulate the flow of information and enable the model to retain or discard data as needed. Such gate mechanism has shown exceptional performance in processing short-term time series data. While LSTMs still face challenges when modeling very long-term dependencies. As sequence lengths increase, the memory cell's capacity may become insufficient to retain all crucial information, causing long-term dependencies to fade or be overwritten [72]. BiLSTM extends the standard LSTM framework by processing data in both forward and reverse directions, thus providing a richer contextual understanding and improving performance on tasks where the future context is as important as the past [73].

Transformer is an emerging deep learning model architecture designed to process time series data. It typically consists of an encoder-decoder framework: (1) the encoder maps input sequences to a latent representation, and (2) the decoder generates output sequences by selectively attending to relevant parts of the input using multi-head self-attention and feed-forward layers. Transformer leverages self-attention mechanisms to learn temporal dependencies globally without relying on recurrent structures [74]. These self-attention mechanisms operate on the entire sequence simultaneously, which enables efficient parallel

processing and excels at capturing long-term dependencies. In addition, the complex structure of Transformer poses challenges for convergence and necessitates large amounts of data for effective training.

2.4. Explainability in time series models

Saliency methods (such as integrated gradients (IG) [75], Vanilla Saliency [76], and smoothGrad [77]) have developed to enhance the explainability of deep neural networks (DNNs) [78]. Vanilla Saliency computes the gradient of the output class score with respect to the input image to evaluate the sensitivity of the model's prediction to pixel-level changes [79, 80]. The resulting heatmaps, referred to as saliency maps, visually represent the importance of each pixel in the model's decision-making process. IG calculates the importance of each pixel by accumulating gradients along a straight-line path from a reference input to the target input [75]. SmoothGrad is a refined variant of Vanilla Saliency and calculate saliency maps by averaging gradients obtained from multiple noisy perturbations of the input [77]. These methods are generally considered post-hoc and model-agnostic: post-hoc means they generate explanations after the model is fully trained [81], and model-agnostic indicates they can be applied to any differentiable model [82]. When applying saliency methods to time series data, previous studies have shown that the intricate sequential dependencies can result in misleading identification of the importance of time steps [83, 84]. Temporal saliency rescaling (TSR) technique has been proposed to adapt IG to time series data. This technique first calculates the time-relevance score for each time by computing the total change in saliency values if that time step is masked; then in each time-step calculate the feature-relevance score for each feature by computing the total change in saliency values if that feature is masked. The final (time, feature) importance score is the product of associated time and feature relevance scores [83]. As such, IG-based TSR enables the generation of high-quality explanations to identify key features as well as key time steps.

3. Methods

3.1. Radiomic sequence modelling

The overall design of the proposed radiomic sequence modelling for the lung ventilation quantification is shown in Fig. 1. The 3D lung volume at each phase of the 4DCT image was first segmented, as shown in Fig. 1(A). The radiomic filtering technique was systematically applied across all respiratory phases using a 3D sliding window approach to capture locoregional intensity and texture patterns throughout the entire lung volume, as shown in Fig. 1(B). Specifically, for each 4DCT phase, a predefined 3D kernel traversed the lung volume with single-voxel step precision. At each lung voxel tomographic coordinate, a cubic sub-volume was defined to extract radiomic intensity and texture features. Each voxel coordinates within the 3D lung volume thus can be represented as an n -dimensional feature vector, and the feature space can be represented as a set of 3D feature maps. As illustrated in Fig. 1(B), the radiomic map retains the same matrix dimensions as the corresponding CT images. Such radiomic filtering procedure was applied consistently across the entire respiratory phases. Therefore, for a given radiomic feature at a given lung voxel tomographic coordinate, the evolution of radiomic feature values throughout the respiratory cycle can be conceptualized as a spatiotemporal-continuous *radiomic sequence* Φ . The dynamic changes in Φ represent the evolution of locoregional lung intensity and texture along respiratory motion and deformation. The red and pink waves in Fig. 1(B) and (C) showed two examples of the obtained radiomics sequences for a given voxel tomographic coordinate in the left upper lung.

Mathematically, let \mathbf{T} represents the collection of all T time step during respiratory cycle, i.e., $\mathbf{T} = 1, 2, \dots, T$, and \mathbf{N} be the collection of all N extracted radiomic features, i.e., $\mathbf{N} = 1, 2, \dots, N$. For a given lung voxel tomographic coordinate (x, y, z) , f_n^t is the value of feature n ($n \in \mathbf{N}$) at time t ($t \in \mathbf{T}$). The radiomic feature vector at time t , denoted θ_t , can be formally represented as:

$$\theta_t = \{f_n^t\}_{n \in \mathbf{N}} \quad (1)$$

The spatiotemporal-continuous radiomic sequence for feature n , denoted Φ_n , can be defined as:

$$\Phi_n = \{f_n^t\}_{t \in \mathbf{T}} \quad (2)$$

Therefore, each voxel at (x, y, z) can be characterized by N radiomics sequences, i.e., $\Phi = \{\Phi_n\}_{n \in \mathbf{N}}$.

Therefore, the feature space \mathcal{F} for each patient can be represented as:

$$\mathcal{F} = (\Phi_{xyz}) \in \mathbb{R}^{X \times Y \times Z} \quad (3)$$

where $X \times Y \times Z$ is the 3D space coordinate of the entire lung volume.

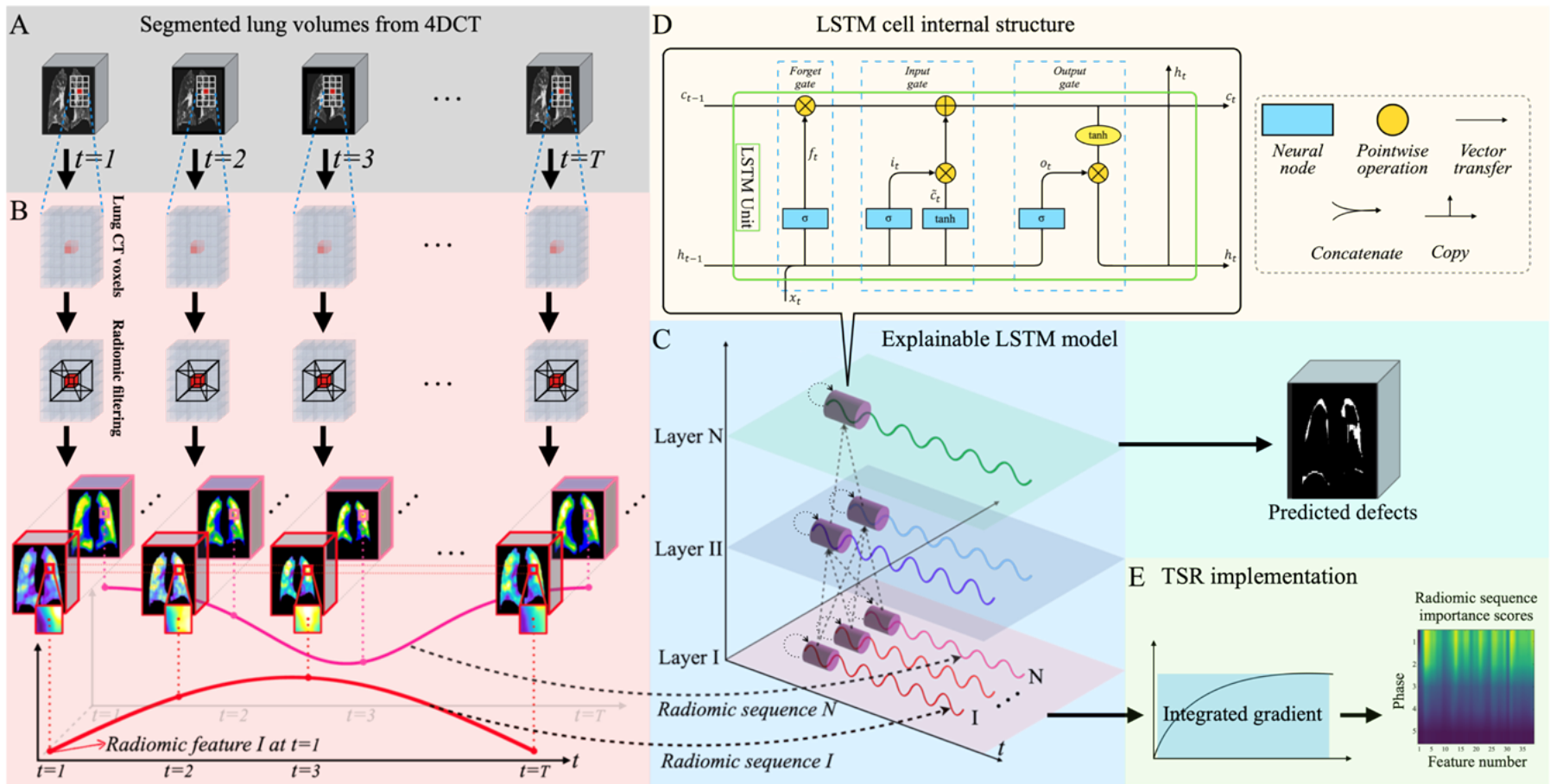


Fig. 1. The overall design of explainable radiomic sequence model. (A) Segmented lung volumes from 4DCT images. (B) The evolution of the radiomic feature at each voxel coordinate throughout the respiratory cycle can be modelled as a radiomic sequence (e.g., as presented by red wave). (C) Explainable LSTM model implementation for ventilation defects identification. The purple cylinders represent the LSTM cells in recurrent layers. (D) The internal structure of the LSTM cell. (E) TSR implementation for identifying key radiomic sequences and key time steps.

In this study, a total of $N = 56$ radiomic features were studied to capture the locoregional lung intensity and texture characteristics [85, 86]. These features can be summarized by three categories:

- 1) 18 Intensity-based features: quantify pixel intensity distribution across the image.
- 2) 22 Gray level co-occurrence matrix (GLCOM)-based features: describe fine texture features in the image, characterize high-resolution heterogeneity, and quantify the frequency of co-occurring adjacent voxel pairs with the same grayscale intensity in a specified direction [87].
- 3) 16 Gray level run-length matrix (GLRLM)-based features: describe coarse texture features in the image, characterize low-resolution heterogeneity, and quantify the distribution of consecutively occurring intensity values of the same gray level in a specified direction [88].

The detailed list of 56 radiomic features was provided in [Table 1](#).

Feature selection was implemented to remove the redundant features and prevent the potential overfitting. Following previous radiomic feature selection studies [89, 90], the process of feature selection in this study encompassed three steps:

- 1) Pearson correlation analysis [91] was performed on radiomic maps at each time t to identify inter-feature correlations, which yielded a correlation matrix for each time step t . The average correlation matrix was derived by averaging all obtained correlation matrices.
- 2) Hierarchical clustering was applied to the average correlation matrix to group features into well-separated clusters based on distance [92]. Similar or highly correlated features were positioned closer in the resulting dendrogram. A total of \tilde{N} clusters were determined based on a specific distance threshold (i.e., cut-off value); features whose distances were below this threshold were considered as one cluster.
- 3) Spearman correlation [93] was used to select representative features. Within each cluster, the feature that demonstrated the highest Spearman correlation with the measured ventilation was selected to form \tilde{N} representative features for following analysis.

Table 1
Fifty-six radiomic features included in this study.

Intensity-based features	1	Mean	Gray level co-occurrence matrix (GLCOM)-based features	29	Inverse Difference	
	2	Variance		30	Inverse Difference Moment	
	3	Skewness		31	Info Measure Correlation 1	
	4	Intensity histogram kurtosis		32	Info Measure Correlation 2	
	5	Median		33	Inverse Difference Moment Normalized	
	6	Minimum grey level		34	Inverse Difference Normalized	
	7	10th percentile		35	Inverse Variance	
	8	90th percentile		36	Joint maximum	
	9	Maximum grey level		37	Sum Average	
	10	Interquartile range		38	Sum Entropy	
	11	Range		39	Sum Variance	
	12	Mean absolute deviation		40	Joint Variance	
	13	Robust mean absolute deviation		Gray level run-length matrix (GLRLM)-based features	41	Short Run Emphasis
	14	Median absolute deviation			42	Long Run Emphasis
	15	Coefficient of variation			43	Gray Level Non-Uniformity
	16	Quartile coefficient of dispersion			44	Gray Level Non-Uniformity Normalized
	17	Energy			45	Run Length Non-Uniformity
	18	Root mean square			46	Run Length Non-Uniformity Normalized
Gray level co-occurrence matrix (GLCOM)-based features	19	Auto Correlation	47	Run Percentage		
	20	Cluster Prominence	48	Low Gray Level Run Emphasis		
	21	Cluster Shade	49	High Gray Level Run Emphasis		
	22	Cluster Tendency	50	Short Run Low Gray Level Emphasis		
	23	Contrast	51	Short Run High Gray Level Emphasis		
	24	Correlation	52	Long Run Low Gray Level Emphasis		
	25	Differential Entropy	53	Long Run High Gray Level Emphasis		
	26	Dissimilarity	54	Gray Level Variance		
	27	Joint Energy	55	Run Length Variance		
	28	Joint Entropy	56	Run Entropy		

3.2. Explainable LSTM Model Design

Given the symmetry in the respiratory cycle, the radiomic sequences extracted from 4DCT may contain symmetrical information. LSTM might be deemed more appropriate than BiLSTM for analyzing temporal dependencies in this scenario, due to its more focused approach on forward-sequence data[94]. Additionally, LSTM is adequate for short time sequences (4DCT only captures 5 or 10 phases in our study), which helps to conserve computational resources. A specially designed LSTM model was developed to associate the radiomic sequences Φ with measured ventilation defects, as shown in Fig. 1(C). The application of BiLSTM was also further explored in subsequent ablation studies detailed in section 4.2. The developed LSTM model consisted of 5 recurrent layers with decreasing numbers of LSTM cells: 128, 64, 32, 16, and 8, respectively. LSTM cell (Fig. 1D) consists of three gates: the input gate, i_t , the forget gate, f_t , and the output gate, o_t . The hidden state h_t of an LSTM cell at time step t is updated by integration of the input θ_t , input gate i_t , forget gate f_t , output gate o_t , cell state c_t , and hidden state h_{t-1} at preceding time step $t - 1$ [64, 95]. As shown in the Fig. 1(D), The forget gate f_t modulates the retention of the previous cell state c_{t-1} , determining how much of the past information is carried forward. The input gate i_t governs the extent to which this new candidate information is incorporated into the cell state c_t . The output gate o_t dictates how much of the cell state c_t is used to compute the hidden state h_t through an element-wise product with the hyperbolic tangent of c_t . In this process, the LSTM cell selectively remember or forget information, updates the hidden state to control how information flows in and out of the internal states of the network [96, 97]. In the first recurrent layer, a series of hidden states (i.e., hidden state sequence) was derived, which can be denoted as $\mathbf{H} = \{h_1, h_2, \dots, h_t\}$. The recurrent layer learns characteristics of radiomic sequences from different aspects at each time step t , thereby capturing the time dependencies [95]. The subsequent 4 recurrent layers adhered to a similar design, and the input of each layer was the hidden state sequences \mathbf{H} derived from the previous layer. A dense layer with a sigmoid activation function was finally employed to generate the binary classification prediction (i.e., lung defects or healthy lung).

The Temporal Saliency Rescaling (TSR) technique was subsequently employed to explain key radiomic sequences and key time steps in the ventilation defects identification, which is built upon the integrated gradient (IG) technique [98], as shown in Fig. 1(E). Let function $L : \mathbb{R}^{\tilde{N} \times T} \rightarrow [0,1]$ represents our neural network, $\bar{\Phi} \in \mathbb{R}^{\tilde{N} \times T}$ be the baseline input (i.e., a zero-embedding matrix considered as a non-informative reference point). Consider the straight-line path from the baseline $\bar{\Phi}$ to the input Φ and

compute the gradients at all points along the path. IG is obtained by cumulating these gradients and is defined as the following equation:

$$IG(\Phi) = (\Phi - \bar{\Phi}) \cdot \int_{\alpha=0}^1 \frac{\partial L(\bar{\Phi} + \alpha(\Phi - \bar{\Phi}))}{\partial \Phi} d\alpha \quad (4)$$

where α is the interpolation parameter. IG quantifies the cumulative contribution of the input in the model prediction from the baseline state $\bar{\Phi}$ to the actual state Φ [98]. Based on the IG technique, TSR decouples the feature importance analysis into assessments of time relevance scores \mathbf{S}^{time} and feature relevance scores $\mathbf{S}^{feature}$ to identify the key radiomic sequences [83]. Time relevance scores \mathbf{S}^{time} were assessed by observing the IG changes when specific 4DCT time step was omitted. Specifically, to calculate the time relevance score at time step t , Φ^t is defined by setting $\theta_t = 0$ in Φ . By substituting Φ and Φ^t separately into Eq. (4) and calculating the difference, the time relevance score S_t for time step t was obtained as follows:

$$S_t = |IG(\Phi) - IG(\Phi^t)| \quad (5)$$

By implementing Eq. (5) on each time step, the time relevance scores \mathbf{S}^{time} were obtained (i.e., $\mathbf{S}^{time} = \{S_{t=1}, S_{t=2}, \dots, S_{t=T}\}$). Similarly, feature relevance scores $\mathbf{S}^{feature}$ were assessed by observing the IG changes when specific radiomic feature was omitted. Specifically, to calculate the feature relevance score of radiomic feature n , Φ^n is defined by setting $\Phi_n = 0$ in Φ . By separately substituting Φ and Φ^n into Eq. (4) and calculating the difference, the feature relevance score $S_n^{feature}$ of radiomic feature n was obtained as follows:

$$S_n = |IG(\Phi) - IG(\Phi^n)| \quad (6)$$

By computing Eq. (6) on each radiomic feature, the feature relevance scores $\mathbf{S}^{feature}$ were obtained (i.e., $\mathbf{S}^{feature} = \{S_{n=1}, S_{n=2}, \dots, S_{n=\tilde{N}}\}$). The temporal saliency map can be derived by taking the outer product of time relevance scores \mathbf{S}^{time} and feature relevance scores $\mathbf{S}^{feature}$:

$$Temporal\ saliency\ map = \mathbf{S}^{feature} \cdot (\mathbf{S}^{time})^T \quad (7)$$

The horizontal axis of the map represents the feature index from 1 to \tilde{N} , the vertical axis of the map represents the time step from 1 to T . The element at coordinate (n, t) of the temporal saliency map is the product of S_n and S_t , and represents the quantified importance score for corresponding feature f_n^t . The

importance score of radiomic sequence Φ_n was derived by averaging the importance scores of all features f_n^t within Φ_n across all voxel samples. The key radiomic sequences were identified through the analysis of the radiomic sequence importance score histogram.

4. Experiments and results

4.1. Imaging dataset

This study utilized a public lung cancer patient dataset from the Ventilation And Medical Pulmonary Image Registration Evaluation (VAMPIRE) Dataset [9]. The VAMPIRE dataset comprises paired image acquisitions of CT and reference ventilation images (RefVI), encompassing 25 individuals with Galligas-PET/CT imaging and 20 with DTPA-SPECT/CT imaging. The respiratory phases were processed from exhalation to inhalation. The 4DCT images were reconstructed into 5 and 10 respiratory phases for PET and SPECT groups, respectively. The original resolutions of 4DCT images for PET and SPECT groups were $1.07 \text{ (mm)} \times 1.07 \text{ (mm)} \times 5.00 \text{ (mm, slice thickness)}$ and $0.97 \text{ (mm)} \times 0.97 \text{ (mm)} \times 2.0, 2.5, \text{ or } 3.0 \text{ (mm, slice thickness)}$, respectively. All these 4DCT images were acquired under free-breathing conditions. Reference lung ventilation images (RefVIs), i.e., PET and SPECT images, were registered to the corresponding time-averaged 4DCT. Lung masks were provided for each phase of the 4DCTs and corresponding RefVIs of each patient. All 4DCT images and RefVIs were resampled with $2 \times 2 \times 2 \text{ mm}^3$ isotropic voxel size for the following analysis. Following the original VAMPIRE studies, the ground truth pulmonary defects were identified as follows: (1) voxels with ventilation intensity above ± 4 standard deviations of the mean intensity of overall RefVI lung voxels were removed until the threshold converged to within 1% of the last threshold [9, 99]; (2) the region with the lowest 30% of the total

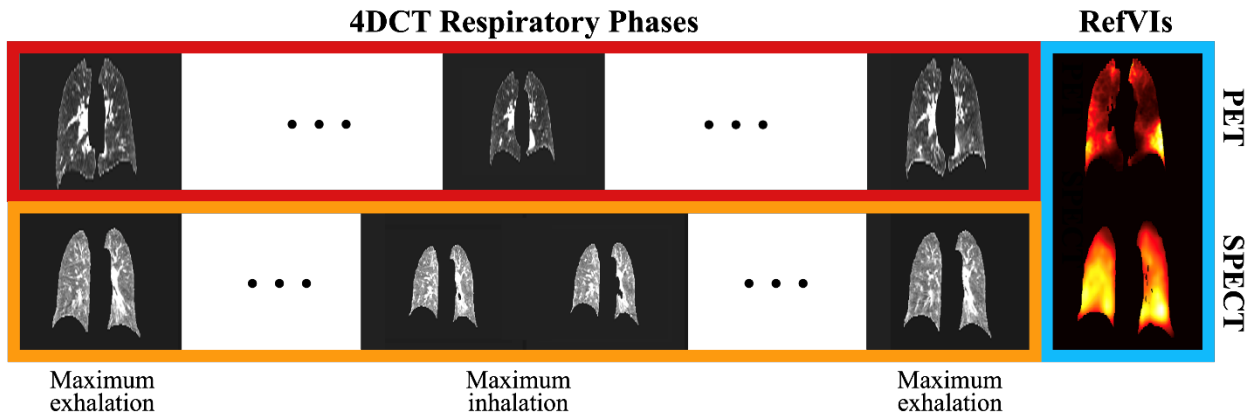


Fig. 2. Visual inspection of RefVI and 4DCT images. The upper row represents PET/CT, and the lower row represents SPECT/CT. The respiratory phases depict range from a maximum exhalation to the subsequent maximum exhalation.

intensity in PET/SPECT is considered as the ground truth pulmonary defects [9, 50]. Fig. 2 provides a visual representation of the dataset.

4.2. Ablation studies

The ablation study was conducted to rigorously the contributions of each component of the neural radiomic sequence model. Specifically, each individual component of the proposed neural radiomic sequence model was removed or modified to assess their impact on the overall performance in identifying ventilation defects. Three variants of the neural radiomic sequence model were produced:

- In the first variant, LSTM with 4DCT images was evaluated: the radiomic sequence modelling component was excluded and the raw 4DCT images served as the LSTM model input. Specifically, the LSTM depicted in Fig. 1(C) was employed to identify ventilation defects by utilizing the changing voxel intensity values across respiratory phases as the sole feature input. This variant determined the impact of removing the detailed locoregional manual-defined image intensity and texture information.
- In the second variant, BiLSTM with radiomic sequences was evaluated: the LSTM model in Fig. 1(C) was replaced by a BiLSTM. This variant assessed the model performance between LSTM and BiLSTM. Building on the LSTM model depicted in Fig. 1(C), the BiLSTM model consisted of two such LSTM components: a forward LSTM and a backward LSTM. The forward component processes the input sequence from beginning to end. The backward component processes the input sequence from end to beginning. In each direction, the processing of radiomic sequences was modeled as a recurrent process with its own hidden state [100]. The bidirectional hidden states were concatenated, and a dense layer with a sigmoid activation function was applied to this concatenated state to generate the prediction of ventilation defects.
- In the third variant, Transformer with radiomic sequences was evaluated: the explainable LSTM model in Fig. 1(C) was replaced by a Transformer encoder. This variant assessed the performance between LSTM and Transformer encoder. The Transformer encoder was composed of positional encoding and four identical transformer encoder blocks. A fixed sinusoidal positional encoding scheme was applied to the input before they are fed into the encoder to mark the inherent sequential order in the input data [101]. Each encoder block consisted of a multi-head self-attention layer (4 attention heads) to dynamically attend to distinct regions of the input sequence [101] and a feed-forward neural network layer to enhance discriminative feature representations. Additionally, residual connections were incorporated after each encoder block, which directly

added the original input of the layer to its output. This design aimed to preserve input information and improve gradient flow[102]. The ventilation defects were predicted by adopting a dense layer with sigmoid activation.

Each of these variants was evaluated and compared to the neural radiomic sequence model to assess their relative performance in identifying ventilation defects. The detailed evaluation metrics are presented in section 4.5.

4.3. Comparison studies

To investigate the defects identification performance of the neural radiomic sequence model, another four machine/deep learning-based models were investigated:

- **U-Net with original 4DCT:** the prediction model based on U-Net using the original 4DCT images as input. The U-Net model in this study was composed of an encoding part and a decoding part. The encoding part contained four convolutional blocks; each block contains two $3\times 3\times 3$ convolutional layers, followed by a rectified linear unit (ReLU) activation and a $2\times 2\times 2$ max pooling operation. In this process, the spatial dimension of the input image was reduced, while the number of feature maps increased. The decoding part is composed of four up-convolutional blocks. Each block in this part included a $2\times 2\times 2$ transposed convolution to up-sample the feature maps, a concatenation with high-resolution features from the encoding part to combine the feature and spatial information, and a convolutional block to refine the representation. As such, the feature maps were up-sampled to match the original image size. The ventilation defects were predicted by adopting a $1\times 1\times 1$ convolutional layer with sigmoid activation.
- **U-Net++ with original 4DCT:** the prediction model based on U-Net++ using the original 4DCT images as input. Building on the U-Net model, U-Net++ added additional skip connections between the intermediate convolutional blocks of the encoding and decoding parts [103]. Features from earlier blocks in the encoder were not only connected to their corresponding blocks in the decoder but also to multiple blocks in the decoder (e.g. features from the first block in the encoder were connected to the first, second, third, and fourth blocks in the decoder). This approach enabled a more robust feature extraction, refined feature fusion, and reconstruction process [103]. The ventilation defects were predicted by adopting a $1\times 1\times 1$ convolutional layer with sigmoid activation.
- **Res-UNet with original 4DCT:** the prediction model based on Res-UNet using the original 4DCT images as input. Building on the U-Net model, the Res-UNet model introduced residual

connections into both the encoding and decoding parts (i.e., all convolution blocks were replaced by residual blocks) [102]. The residual block consists of two $3 \times 3 \times 3$ convolutional layers, followed by ReLU activation functions and a $2 \times 2 \times 2$ max pooling operation. Unlike the convolutional block, the input to each residual block is directly added to the output of the second convolutional layer via a skip connection. The residual operation allowed the network to learn identity mappings and helped preserve information of input data, which enhanced the ability of capturing discriminative features while mitigating the vanishing gradient problem [102]. The ventilation defects were predicted by adopting a $1 \times 1 \times 1$ convolutional layer with sigmoid activation.

- **Random forest with original 4DCT:** the prediction model based on random forest (RF) using the original 4DCT images. RF is a typical machine learning model that adopts a hierarchical tree structure [104]. Each internal node represents a decision based on a specific input variable, while each leaf node provides a prediction for the output variable. For each voxel, the intensity values at different time steps served as different input features. These features were fed into the RF model to predict whether the voxel represented a ventilation defect.

4.4. Implementation details

The radiomic filtering settings adhered to the previous lung radiomic filtering studies: (1) the intensity-based features were extracted directly from the lung volume images [85], (2) a fixed bin number (=64) image discretization was adopted to calculate the second-order features (i.e., GLCOM-based and GLRLM-based features) [45], and (3) a $26 \times 26 \times 26 \text{ mm}^3$ sized kernel was employed for effective regional feature extraction [38, 105]. All 56 radiomic features were averaged over 13 directions [106] to approximate rotational invariance [42, 88, 107, 108]. All the radiomic filtering calculations were performed using an in-house developed radiomics filtering toolbox with MATLAB (MATLAB R2023a; MathWorks, Natick, Ma). The toolbox has been comprehensively validated against the image biomarker standardization initiative (IBSI) standardization [109] and the digital phantoms [110]. Additionally, the toolbox has been specifically optimized for voxel-based, rotationally invariant calculations in 3D spaces [45]. The optimization enhancements encompassed two main areas: (1) fully vectorized calculation procedures for efficient small-kernel matrix manipulation, and (2) the application of parallel computing techniques to accelerate distributed computations.

For deep learning models, training was conducted for up to 500 epochs using the Adam optimization algorithm with a learning rate of 0.0001 and a gradient clipping value of 1.0. To mitigate overfitting, early

stopping was applied. The binary cross-entropy loss function was used across all models. Batch size settings varied based on the model architecture. For U-Net with 4DCT, U-Net++ with 4DCT, and Res-UNet with 4DCT, batch size was set as 16. For Neural radiomic sequence model, LSTM with original 4DCT, BiLSTM with radiomic sequences, and Transformer with radiomic sequences, batch size was set as 2048. For random forest (RF) with 4DCT, the hyperparameters were optimized using random search, and training was conducted using 100 decision trees, the Gini impurity criterion, bootstrap sampling, and parallel execution across 16 CPU cores.

All the calculations were carried out in Python 3.7 with 16 Core Intel Core i7-13700KF CPU @ 3.4 GHz, 128GB DDR4 memory ($4 \times 32\text{GB}$ @ 3200 MHz), and Nvidia GeForce RTX 4070 Card. The TSR technique was implemented with TSInterpret Library [111].

4.5. Evaluation metrics

The quality of hierarchical clustering was evaluated using the Cophenetic Correlation Coefficient (CC) [112]. A CC value above 0.75 indicates that the dendrogram produced by the hierarchical clustering accurately represents feature distances [89]. The optimal cut-off value was determined by the highest silhouette coefficient (SC) value [113], where an SC value above 0.7 indicates better cluster compactness and separation [114].

The models in all comparative studies were evaluated on 25 PET and 20 SPECT cases using the Dice index, AUCROC, sensitivity, and accuracy with five-fold cross-validation. Wilcoxon signed-rank test on all evaluation metrics with a significance level of 0.01 was adopted.

4.6. Results of feature selection

Fig. 3 exhibited the feature correlation heatmap after hierarchical clustering. The heatmap visualized the correlations between different features using color gradations. The intensity of the color reflects the strength of the correlation, ranging from 1 (indicating positive correlation, shown in blue) to -1 (indicating negative correlation, shown in red). The hierarchical clustering dendrogram illustrated the clustering relationships among features, with a CC value of 0.80 (>0.75). Features with higher correlation were positioned closer together in the dendrogram. The cut-off value ($=0.02$) with the highest SC value of 0.79 (>0.7) was utilized to categorize 38 feature clusters. In each cluster, the feature exhibiting the highest Spearman correlation with the ground truth was finally selected, thereby 38 features were finally selected.

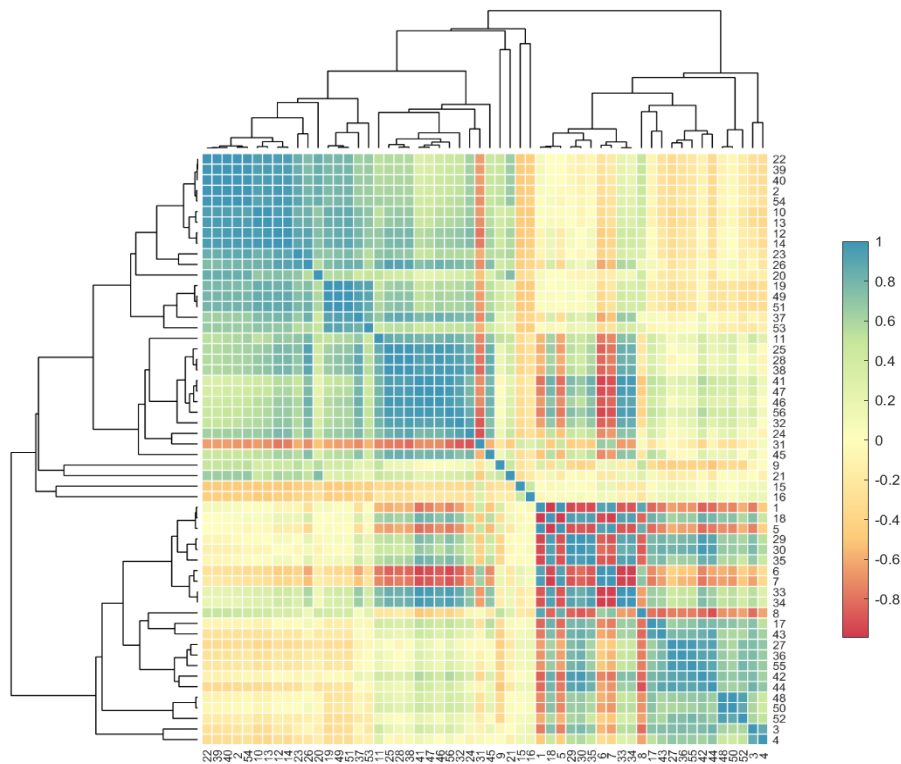


Fig. 3. The feature correlation heatmap after hierarchical clustering. The number of x or y axis represents the feature number. The intensity of the color indicates the strength of the correlation between two features, ranging from 1 (indicating positive correlation, shown in blue) to -1 (indicating negative correlation, shown in red). The dendrogram on the left side or top of the heatmap display the clustering relationship between features. Features that were more highly correlated were positioned closer together in the dendrogram.

4.7. Results of ventilation defects prediction

Fig. 4 to 9 illustrated examples of predicted binary ventilation defects from the proposed neural radiomic sequences model, alongside other comparative models. Part A of these figures showed original RefVI and the identified lung defects regions by thresholding the lowest 30% of the total intensity of the RefVI. Part B presented the corresponding 4DCT images from maximum exhalation to the subsequent maximum exhalation. Part C exhibited the predicted defects from all comparative models. Fig. 4 to 6 were examples from SPECT cases, and Fig. 7 to 9 were from PET cases. The binary predictions from our model successfully identified lung defects and exhibited high visual consistency with the ground truth. The binary predictions from BiLSTM model and Transformer model were similar to those from our model, whereas predictions from other models exhibited low consistency with the ground truth. Additionally, some overestimations at the lung margins could be observed in the binary predictions derived from our model.

Table 2 summarized the Dice index, sensitivity, accuracy, and AUCROC from 5-fold cross-validation, and the derived ROC curves were shown in Fig. 10. The proposed neural radiomic sequence model achieved the best prediction performance among the comparative studies. Specifically, for 25 PET cases, the proposed model achieved a mean Dice index of 0.78, an AUCROC of 0.85, a sensitivity of 0.78, and an accuracy of 0.76. For 20 SPECT cases, the proposed model achieved a mean Dice coefficient of 0.78, AUCROC of 0.84, sensitivity of 0.78, and accuracy of 0.74. Additionally, U-Net with original 4DCT (mean Dice = 0.51/0.51 in PET/SPECT, AUCROC = 0.68/0.65, sensitivity = 0.40/0.47, accuracy = 0.67/0.62), U-Net++ with original 4DCT (mean Dice = 0.62/0.57 in PET/SPECT, AUCROC = 0.72/0.69, sensitivity = 0.64/0.63, accuracy = 0.67/0.60), Res-UNet with original 4DCT (Dice = 0.59/0.67 in PET/SPECT, AUCROC = 0.73/0.74, sensitivity = 0.57/0.68, accuracy = 0.68/0.68), RF with original 4DCT (Dice = 0.58/0.52 in PET/SPECT, AUCROC = 0.63/0.67, sensitivity = 0.59/0.48, accuracy = 0.60/0.63), and LSTM with original 4DCT (Dice = 0.69/0.66 in PET/SPECT, AUCROC = 0.77/0.71, sensitivity = 0.65/0.65, accuracy = 0.70/0.63) all showed limited performance. BiLSTM with radiomic sequences (Dice = 0.78/0.78 in PET/SPECT, AUCROC = 0.85/0.84, sensitivity = 0.77/0.77, accuracy = 0.76/0.74) and Transformer with radiomic sequences (Dice = 0.77/0.77 in PET/SPECT, AUCROC = 0.85/0.84, sensitivity = 0.76/0.74, accuracy = 0.77/0.75) had comparable performance to our model.

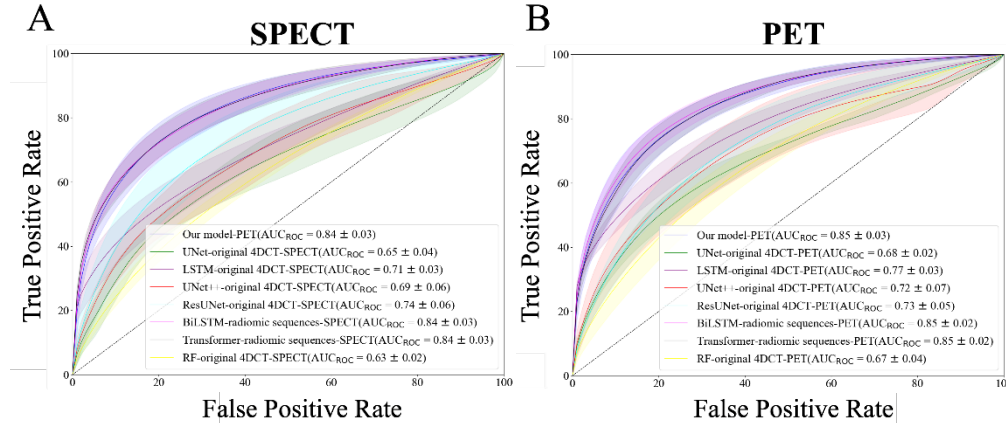


Fig. 10. ROC Curves from our proposed model (blue line), U-Net with original 4DCT (green line), LSTM with original 4DCT (purple line), U-Net++ with original 4DCT (red line), Res-UNet with original 4DCT (cyan line), BiLSTM with radiomic sequences (magenta line), Transformer with radiomic sequences (black line), and RF with original 4DCT (yellow line) in (A) PET cases, and (B) SPECT cases.

Table 2

Five-fold cross-validation ventilation quantification results in all comparative studies. “*” indicates a statistically significant difference compared with results of proposed model.

	Models	Dice	AUCROC	Sensitivity	Accuracy
PET	Our model	0.78(0.74-0.79)	0.85(0.80-0.88)	0.78(0.72-0.83)	0.76(0.72-0.79)
	BiLSTM with radiomic sequences	0.78(0.74-0.79)	0.85(0.81-0.87)	0.77(0.72-0.82)	0.76(0.72-0.78)
	Transformer with radiomic sequences	0.77(0.73-0.79)	0.85(0.81-0.87)	0.76(0.73-0.81)	0.77(0.73-0.79)
	U-Net with original 4DCT	0.51(0.44-0.55)*	0.68(0.65-0.70)*	0.40(0.32-0.44)*	0.67(0.62-0.70)*
	U-Net++ with original 4DCT	0.62(0.55-0.75)*	0.72(0.61-0.80)*	0.64(0.50-0.80)*	0.67(0.58-0.73)*
	Res-UNet with original 4DCT	0.59(0.36-0.69)*	0.73(0.67-0.80)*	0.57(0.24-0.73)*	0.68(0.65-0.74)*
	RF with original 4DCT	0.58(0.48-0.64)*	0.63(0.60-0.65)*	0.59(0.51-0.74)*	0.60(0.57-0.64)*
	LSTM with original 4DCT	0.69(0.65-0.74)*	0.77(0.73-0.80)*	0.65(0.56-0.71)*	0.70(0.66-0.74)*
	SPECT	Our model	0.78(0.74-0.82)	0.84(0.80-0.87)	0.78(0.68-0.86)
BiLSTM with radiomic sequences		0.78(0.73-0.82)	0.84(0.80-0.86)	0.77(0.67-0.84)	0.74(0.71-0.78)
Transformer with radiomic sequences		0.77(0.73-0.82)	0.84(0.80-0.86)	0.74(0.64-0.80)	0.75(0.70-0.78)
U-Net with original 4DCT		0.51(0.40-0.58)*	0.65(0.61-0.70)*	0.47(0.26-0.72)*	0.62(0.58-0.67)*
U-Net++ with original 4DCT		0.57(0.28-0.70)*	0.69(0.59-0.75)*	0.63(0.17-0.88)*	0.60(0.49-0.69)*
Res-UNet with original 4DCT		0.67(0.64-0.69)*	0.74(0.67-0.85)*	0.68(0.58-0.78)*	0.68(0.62-0.69)*
RF with original 4DCT		0.52(0.48-0.57)*	0.67(0.60-0.70)*	0.48(0.42-0.54)*	0.63(0.59-0.67)*
LSTM with original 4DCT		0.66(0.60-0.70)*	0.71(0.66-0.77)*	0.65(0.50-0.82)*	0.63(0.58-0.72)*

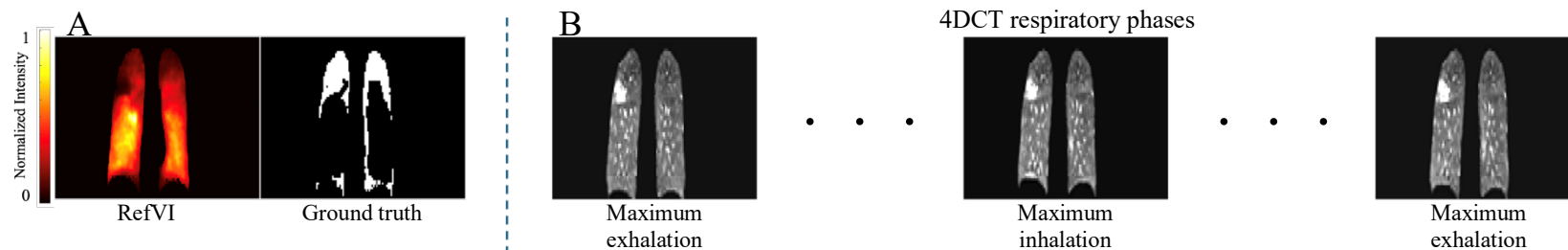


Fig. 4. Example I of (A) original RefVI and identified lung defects regions by thresholding the lowest 30% of the total intensity of the RefVI; (B) corresponding 4DCT from a maximum exhalation to the subsequent maximum exhalation; (C) predicted defects regions from all comparative models.

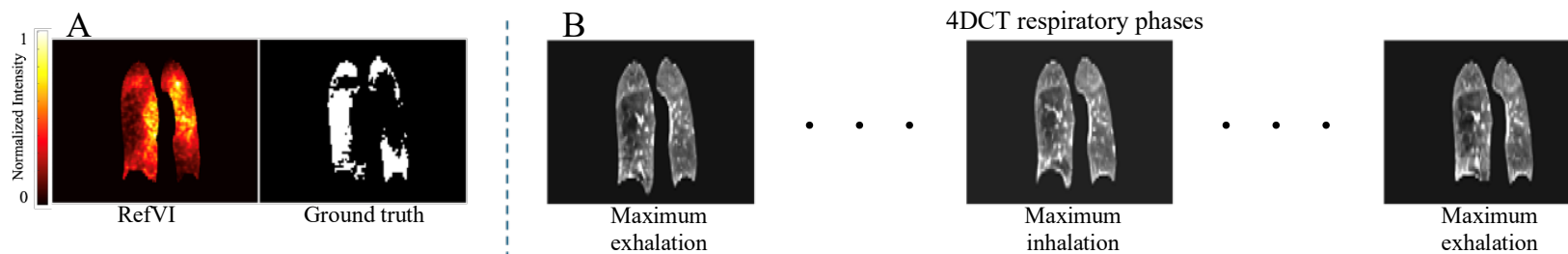


Fig. 5. Example II of (A) original RefVI and identified lung defects regions by thresholding the lowest 30% of the total intensity of the RefVI; (B) corresponding 4DCT from a maximum exhalation to the subsequent maximum exhalation; (C) predicted defects regions from all comparative models.

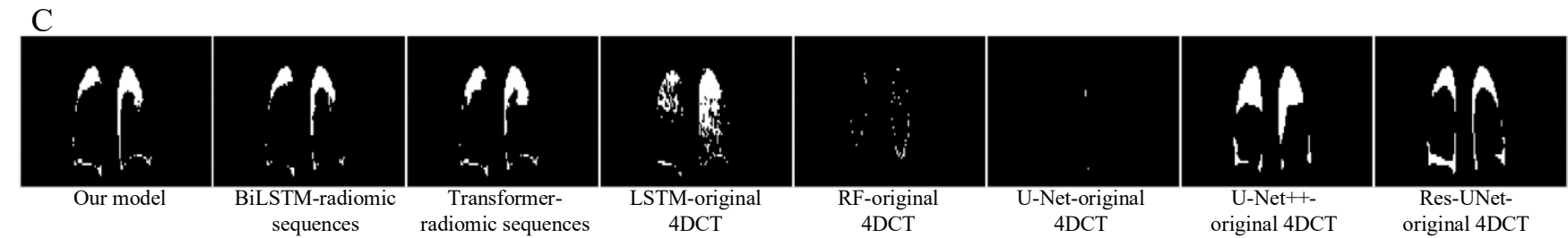
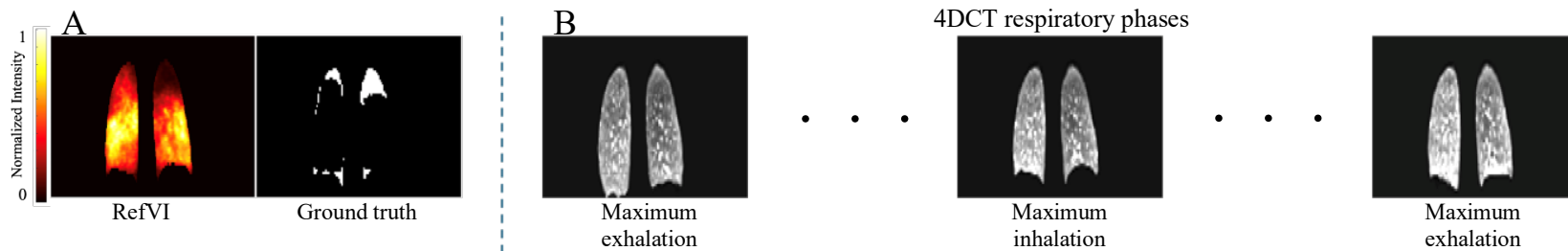


Fig. 6. Example III of (A) original RefVI and identified lung defects regions by thresholding the lowest 30% of the total intensity of the RefVI; (B) corresponding 4DCT from a maximum exhalation to the subsequent maximum exhalation; (C) predicted defects regions from all comparative models.

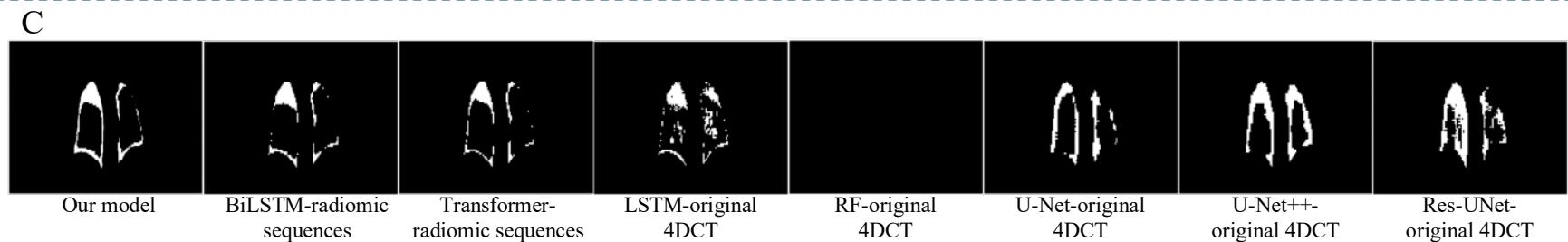
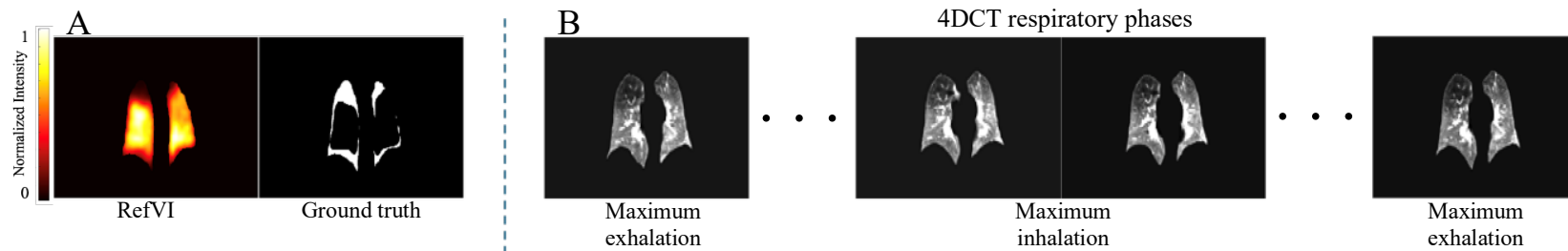


Fig. 7. Example IV of (A) original RefVI and identified lung defects regions by thresholding the lowest 30% of the total intensity of the RefVI; (B) corresponding 4DCT from a maximum exhalation to the subsequent maximum exhalation; (C) predicted defects regions from all comparative models.

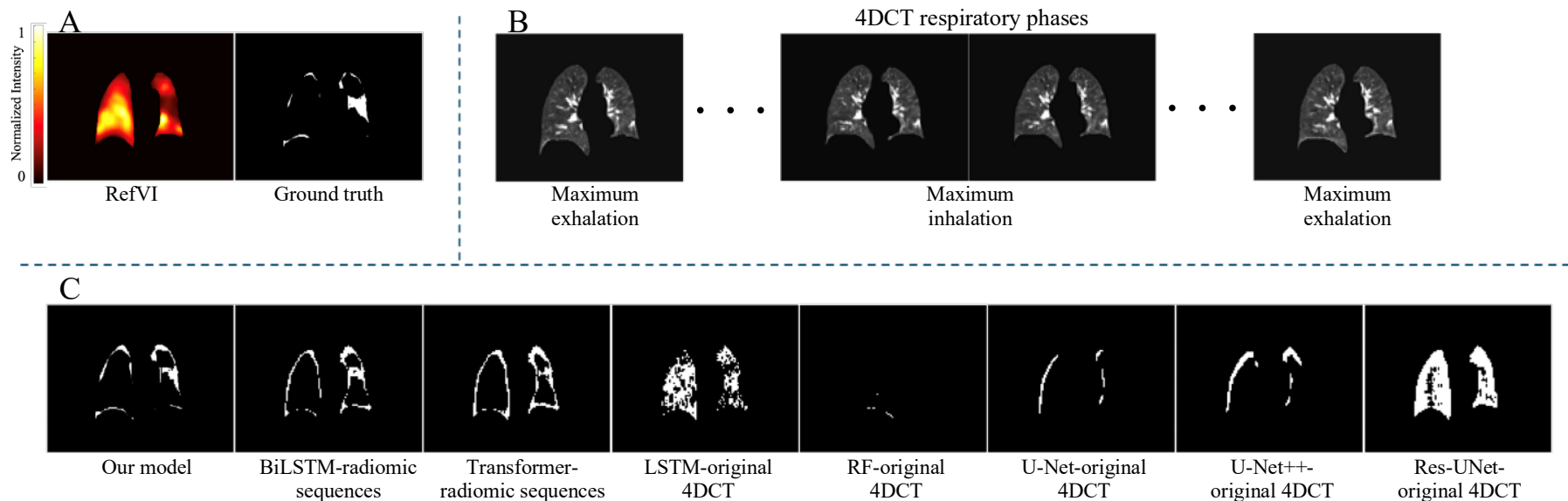


Fig. 8. Example V of (A) original RefVI and identified lung defects regions by thresholding the lowest 30% of the total intensity of the RefVI; (B) corresponding 4DCT from a maximum exhalation to the subsequent maximum exhalation; (C) predicted defects regions from all comparative models.

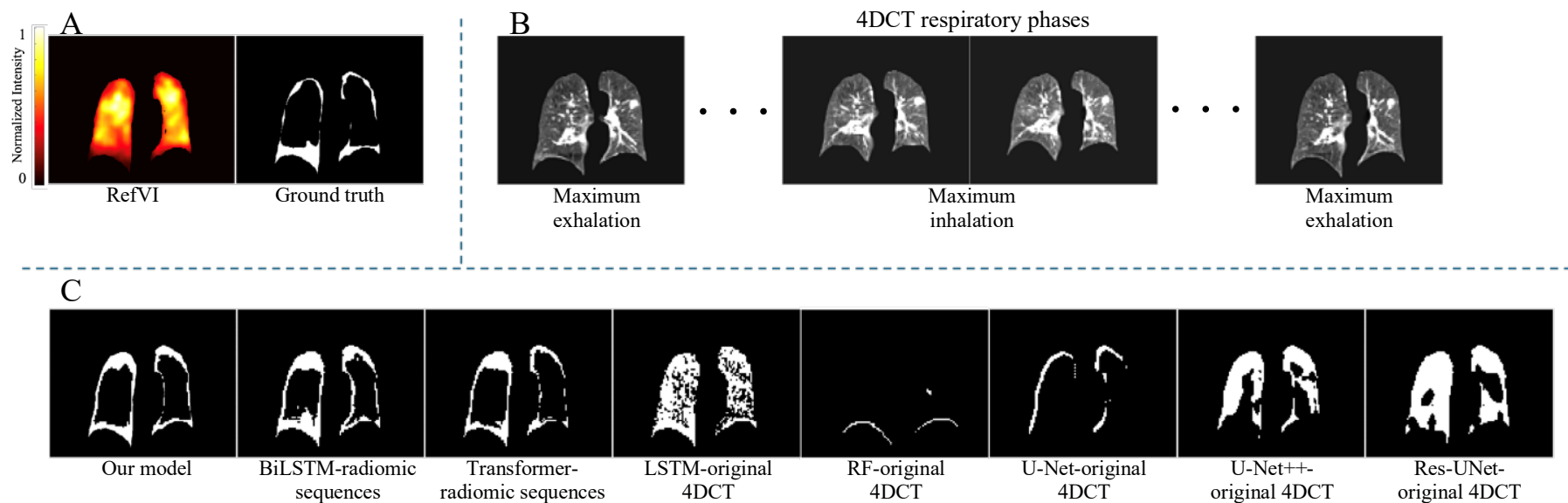


Fig. 9. Example VI of (A) original RefVI and identified lung defects regions by thresholding the lowest 30% of the total intensity of the RefVI; (B) corresponding 4DCT from a maximum exhalation to the subsequent maximum exhalation; (C) predicted defects regions from all comparative models.

4.8. Results of key radiomic sequences and key time steps explanation

The average temporal saliency maps from PET cases and SPECT cases were shown in Fig. 11. The horizontal axis of the map represents radiomic sequence feature number, and the vertical axis represents the respiratory phase. The respiratory phases were demonstrated in the order of maximum exhale, maximum inhale, and maximum exhale. The color in the temporal saliency map corresponds to the feature importance score; more intense colors indicate lower feature importance and brighter colors indicate higher feature importance. The colors of the exhalation phases appeared significantly brighter than those of the inhalation phases, which suggests that the exhalation phases hold greater importance than the inhalation phases.

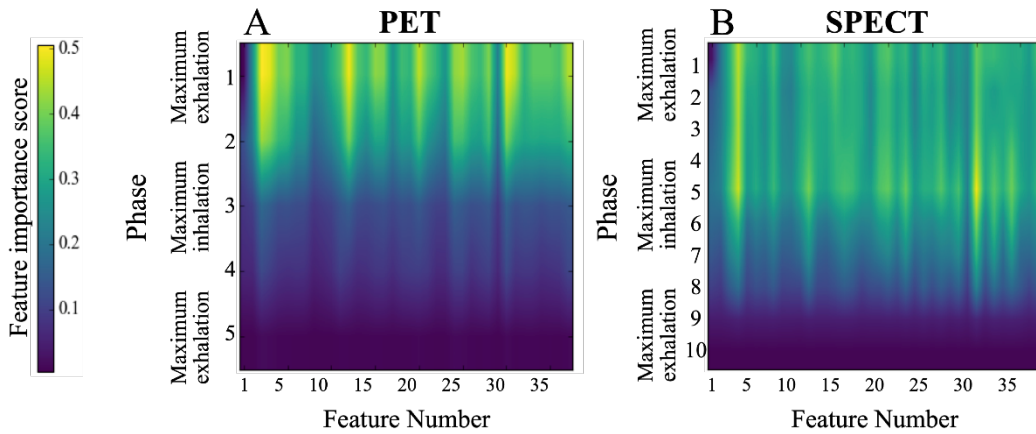


Fig. 11. Average TSMs from (A) PET cases, and (B) SPECT cases. The horizontal axis of the TSM represents radiomic sequence index, and the vertical axis represents the respiratory phase. The color in the TSM corresponds to the importance score; more intense colors indicate lower feature importance and brighter colors indicate higher feature importance.

The histogram depicted in Fig. 12 illustrated the distribution of radiomic sequences importance scores derived from temporal saliency maps. The abscissa denotes the importance scores, while the ordinate indicates the count of radiomic sequences. Three key radiomic sequences represented by the three rightmost bars in the histogram have been discerned as important predictors of ventilation defects, which are *Intensity-based 10th percentile* (#7), *Intensity-based 90th percentile* (#8), and *GLRLM-based Run-Length Non-Uniformity* (#43).

Fig. 13 presented the variation trends of three key radiomic sequences across all lung voxel samples, where red lines/blue lines represent average sequences (along the respiratory phase) for voxels in lung compromised or healthy region, respectively. Similar trends can be observed in PET (shown in Fig. 13A)

and SPECT (shown in Fig. 13B) cases, and distinct trends can be observed for 3 radiomic sequences in lung compromised versus healthy lung regions. Specifically, in healthy lung regions, *Intensity-based 10th percentile* and *GLRLM-based Run-Length Non-Uniformity* remained largely stable. *Intensity-based 90th percentile* exhibited a minimal increase during exhalation and decreased during inhalation. In compromised regions, *Intensity-based 10th percentile* initially rose during exhalation and then declined during inhalation, *Intensity-based 90th percentile* exhibited a slight increase followed by a decrease, and *GLRLM-based Run-Length Non-Uniformity* initially decreased and then increased. These trends suggest that the compromised pulmonary function region typically exhibits an increasing trend of intensity and a decreasing trend of homogeneity (measured by *GLRLM-based Run-Length Non-Uniformity*) during exhalation phases, in contrast to healthy lung tissue. Additionally, both *Intensity-based 10th percentile* and *Intensity-based 90th percentile* in compromised regions were always higher than those in the healthy regions, whereas *GLRLM-based Run-Length Non-Uniformity* in compromised regions was lower than that in healthy regions.

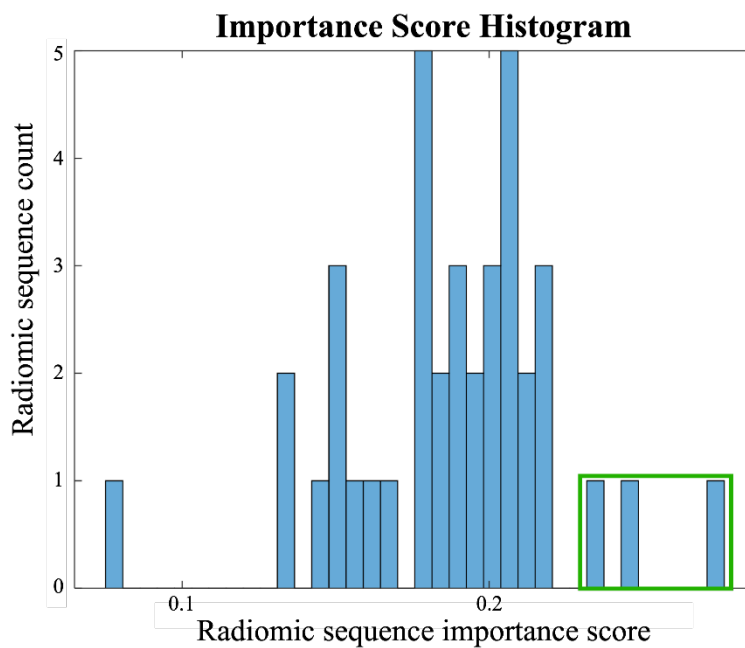


Fig. 12. The histogram of radiomic sequence importance scores. The abscissa denotes the importance scores, while the ordinate indicates the count of radiomic sequences. The green box highlights the radiomic sequences with significantly higher importance.

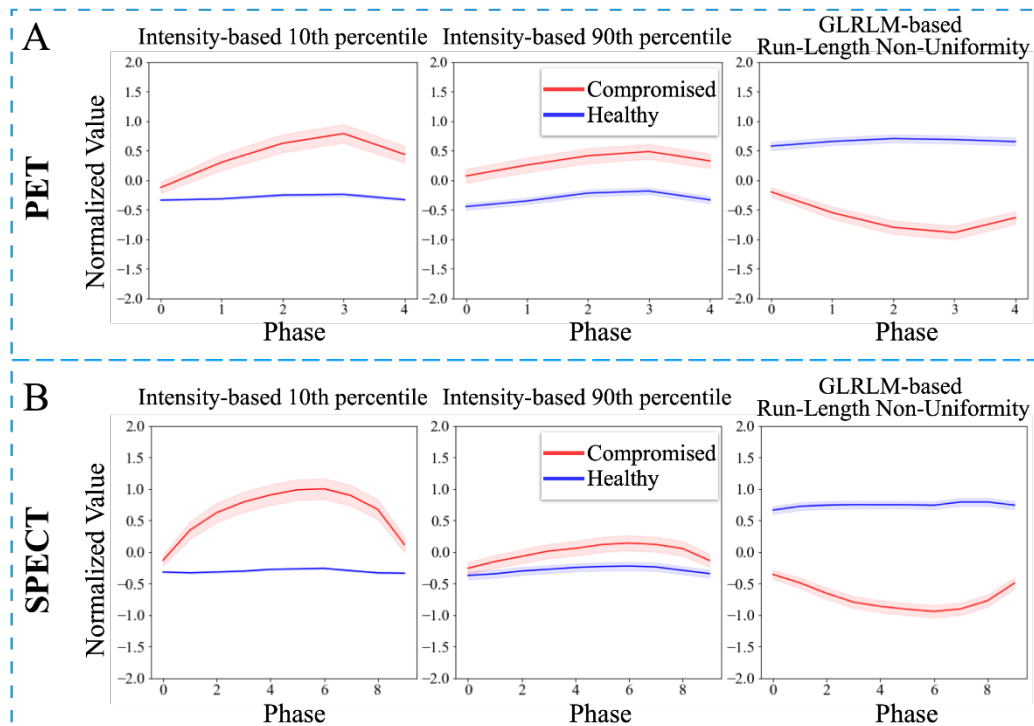


Fig. 13. Trends of key radiomic feature sequences in (A) PET cases, and (B) SPECT cases. Red line represents sequences in compromised region, and blue line represents those in healthy region.

5. Discussion

In this work, we developed an explainable neural radiomic sequence model with spatiotemporal continuity to identify compromised pulmonary ventilation function region using 4DCT images. The key innovation of this work is (1) modelling the locoregional lung texture and intensity heterogeneity changes over the respiratory cycle as spatiotemporal-continuous radiomic sequences, and (2) specifically designing an explainable LSTM model to explain the key radiomic sequences in quantifying the pulmonary ventilation defects. Based on the VAMPIRE dataset, the proposed explainable neural radiomic sequence model showed excellent results in detecting compromised pulmonary function region, with a mean Dice = 0.78/0.78 in 21 PET and 25 SPECT cases. For the other metrics (AUCROC, Accuracy and Sensitivity), there's still a similar phenomenon. The high prediction accuracy of our model suggests that it could serve as a potential complement to existing pulmonary quantification methods.

In the ablation studies, LSTM with original 4DCT (mean Dice = 0.69/0.66 in PET/SPECT) showed limited performance compared to our model, which was largely attributed to the absence of radiomic sequence modeling. Radiomic sequence modeling effectively quantifies locoregional lung texture and intensity heterogeneity changes over the respiratory cycle, which are critical for understanding the distribution of ventilation defects. In contrast, using raw 4DCT as input makes it challenging for the model to learn key discriminative information. BiLSTM with radiomic sequences (Dice = 0.78/0.78 in PET/SPECT) and Transformer with radiomic sequences (Dice = 0.77/0.77 in PET/SPECT) had comparable performance to our model. These results suggested that the LSTM component in our model effectively captures the correlation between radiomic sequences and lung defects, and the use of more complex models (BiLSTM and Transformer) were unnecessary. BiLSTM enhances long-term temporal dependency modeling by incorporating a bidirectional learning manner [94]. Transformer leverages attention mechanisms to capture temporal dependencies globally [74]. Given the limited time steps captured by 4DCT (5 for PET and 10 for SPECT), their long-term temporal dependencies learning capability is not essential in this study. Additionally, these more complex models required more parameters and computational resources, resulting in slower convergence. Emerging imaging and motion tracking technologies, such as Real-Time MRI [115] and surface tracking [116, 117], can acquire detailed respiratory motion data with more time steps. For future research regarding ventilation analysis using this type of data, the ability of BiLSTM and Transformer to capture long-term dependencies makes them promising candidates.

In the comparison studies, several machine/deep learning-based model (1) U-Net with original 4DCT (mean Dice = 0.51/0.51 in PET/SPECT), (2) U-Net++ with original 4DCT (mean Dice = 0.62/0.57 in PET/SPECT), (3) Res-UNet with original 4DCT (mean Dice = 0.59/0.67 in PET/SPECT), (4) RF with original 4DCT (mean Dice = 0.58/0.52 in PET/SPECT) showed limited performance. The traditional U-Net is designed to focus on spatial patterns and emphasize local spatial dependencies between data points [70, 118]. In this study, the U-Net applied to original 4DCT treated the temporal dimension as multi-channel input. During convolution operations, the filters processed each channel's features independently and ignored their temporal dependencies [119], which contributed to limited performance of U-Net with original 4DCT. U-Net++ built upon U-Net by introducing nested and dense skip connections to improve spatial feature learning and enhance feature aggregation [103]. Res-UNet incorporated residual modules into the U-Net architecture, allowing the input signal to bypass convolutional layers and pass directly to subsequent layers [102]. This design enabled the network to learn residual mappings (i.e., the differences between input and output) rather than the output itself, which improved convergence speed and mitigated the vanishing gradient problem [104]. However, neither architecture enhanced the model's ability to learn temporal dependencies, which limited the performance of U-Net++ with original 4DCT and Res-UNet with original 4DCT. For RF with original 4DCT, RF was primarily designed for statistical data and lacked the capability of explicitly learning temporal dependencies [120]. This limitation in capturing critical temporal information contributed to the model's failure to accurately predict lung defects.

Fig. 4 to 9 showed the predicted ventilation defects from all comparative models. The binary predictions from our model, BiLSTM with radiomic sequences, and Transformer with radiomic sequences were similar and exhibited high visual consistency with the ground truth, while predictions from other models (i.e., LSTM with original 4DCT, RF with original 4DCT, U-Net with original 4DCT, U-Net++ with original 4DCT, and Res-UNet with original 4DCT) all showed low consistency with the ground truth. These finds were supported by the statistical results. Some overestimations can be observed in lung margins of these predictions, which was potentially caused by the lung motion during the respiratory cycle. The motion of the lung can cause certain voxel tomographic coordinates in 4DCT at the peripheral lung regions to turn from containing lung tissue to none, leading to abrupt changes in radiomic feature values. This abrupt variation might cause the model to learn that such changes correspond to low-function targets, making it prone to classify such points as low-functioning. This misclassification results in an overestimation of defects in the peripheral regions of the lungs. In the future research, positional encoding marking the edge/non-edge regions in lung can be added to improve the overestimation.

The temporal saliency maps shown in Fig. 11 were generated from the neural radiomic sequence model to explain the key radiomic sequences and key time steps in quantifying the pulmonary ventilation defects. As shown in Fig. 11, features at exhalation generally appeared brighter than those at inhalation, suggesting that the exhalation exhibits greater importance than the inhalation. This can be well explained as exhalation is the inverse of the inhalation and covers the sufficient information to quantify the defects. Three key radiomic sequences were identified using radiomic sequence importance scores derived from the TSMs, which are *Intensity-based 10th percentile* (#7), *Intensity-based 90th percentile* (#8), and *GLRLM-based Run-Length Non-Uniformity* (#43). *Intensity-based 10th percentile* and *Intensity-based 90th percentile* measure the 10th and 90th percentile gray level intensity within the ROI, respectively [107, 121]. The compromised pulmonary function region is closely associated with diffuse alveolar epithelium destruction, capillary damage/bleeding, hyaline membrane formation, alveolar septal fibrous proliferation, and pulmonary consolidation, and these conditions may lead to increased tissue density in the affected areas [122-124]. This increase of density was reflected by higher gray level intensity in compromised regions compared to those in healthy regions, as shown in Fig. 13. Additionally, variations in air content during respiration directly influence these intensity values [48, 125, 126]. During the exhalation, as air was expelled, the compromised regions became denser, resulting in a substantial increase in the 10th percentile intensity value, and a slight increase in the 90th percentile intensity value. In healthy lung regions, although air was expelled, their predominantly air-filled nature resulted in no change in the 10th percentile intensity value, while the 90th percentile intensity value exhibited a minimal increase. During the inhalation, these features displayed trends that mirrored those observed during exhalation. *GLRLM-based Run-Length Non-Uniformity* assesses the distribution of runs over the run lengths within the ROI [107, 127]. Finding from *GLRLM-based Run-Length Non-Uniformity* is consistent with our previous study [45], where a lower value indicates high pulmonary heterogeneity at the voxel location. During exhalation, the compromised regions underwent volume compression, leading to a denser aggregation of compromised tissue in a reduced space, thereby increasing heterogeneity and decreasing *GLRLM-based Run-Length Non-Uniformity* value. During the inhalation, the feature value changed in the opposite direction to that during exhalation. The healthy regions were inherently homogeneous and maintained this homogeneity throughout the respiratory cycle [128, 129]. This characteristic was reflected in the *GLRLM-based Run-Length Non-Uniformity* value, which generally remained stable over the respiratory cycle and were higher compared to that in compromised regions. Overall, these trends and findings suggest that the compromised pulmonary function region typically exhibits an increasing trend of intensity (measured by *Intensity-based 10th percentile* and *Intensity-based*

90th percentile) and a decreasing trend of homogeneity (measured by *GLRLM-based Run-Length Non-Uniformity*) during exhalation phases, in contrast to healthy lung tissue. Our model is capable of comprehensively evaluating and explaining key radiomic sequences, which could aid clinicians in understanding the behavior of the neural network and enhance their confidence in the clinical applications of deep learning.

Currently, the widespread application of 4DCT in radiotherapy planning and respiratory measurement is well-documented [33, 130], and numerous studies also highlight its utility in diagnosing and evaluating lung diseases such as asthma and COPD [131-133]. This underscores the potential of the developed approach for broad applications in clinical settings. One potential application is employed in functional lung avoidance radiotherapy treatment planning. Functional lung avoidance radiotherapy treatment planning utilizes ventilation functional imaging to guide the dose distribution in treatment planning, aiming to deposit higher doses in compromised function regions while reducing the dose delivered to healthy regions to minimize the injury after radiotherapy [134]. Compared to standard ventilation imaging modalities (i.e., SPECT and PET), the developed method requires only image processing of 4DCT scans to obtain ventilation imaging, thereby negating the need for extra scanner time, exposure to ionizing radiation, or any additional inconvenience to the patient. Another potential is used for regional therapeutic response evaluation. Regionally specific therapies, such as bronchial thermoplasty for asthma [135], endobronchial valve therapy [136], and lung volume reduction surgery for chronic obstructive pulmonary disease [137], necessitate obtaining regional information to assess the efficacy of these interventions.

Given the constraints of patient numbers within the dataset, the developed model underwent evaluation on a limited sample size (i.e., 25 PET and 20 SPECT cases). By regarding independent lung voxels as individual samples, the evaluation effectively encompasses millions of samples, significantly enhancing the robustness of the analysis. A 5-fold cross-validation strategy was also adopted to fully utilize the data and ensure a thorough assessment. Further research with larger data may be needed to test our model. Additionally, the SPECT and PET cases showed heterogeneity in respiratory phases and spatial resolution. Despite observing consistent trends in model performance and feature importance explanation between the SPECT and PET cases, cross-modality validation with homogeneous data remains crucial.

6. Conclusion

We developed a novel explainable neural radiomic sequence model with spatiotemporal continuity for identifying compromised pulmonary ventilation function regions based on 4DCT images. The proposed methodology first utilized radiomic sequence modelling to extract local intensity and texture from 4DCT and employed an explainable RNN to quantify the pulmonary ventilation defects. The explainable neural radiomic sequence model has been evaluated on the lung cancer patients from Vampire Challenge dataset and successfully identified compromised pulmonary ventilation function region as well as explained the key radiomic sequences for understanding the underlying model behavior. The developed novel methodology can be generalized to the other respiratory-related spatiotemporal sequence analysis and has the potential for broad applications in the clinical setting.

Declaration of competing interest

The authors declare that they have no known competing financial interests or personal relationships that could have appeared to influence the work reported in this paper.

Acknowledgments

The authors would like to thank Dr. John Kipritidis, Dr. Paul Keall, Dr. Shankar SIVA, Dr. Tokihiro Yamamoto, and Dr. Joseph Reinhardt for sharing the VAMPIRE dataset.

Data Availability

All imaging data used in this study is obtained from the publicly available VAMPIRE dataset [9]. The original data sets can be downloaded via request from the VAMPIRE website: <https://image-x.sydney.edu.au/vampire-challenge/>.

References

1. Schluger, N.W. and R. Koppaka, *Lung disease in a global context. A call for public health action*. Annals of the American Thoracic Society, 2014. **11**(3): p. 407-416.
2. Heron, M.P., *Deaths: leading causes for 2015*. National Vital Statistics Reports, 2017. **66**.
3. Zar, H.J. and T.W. Ferkol, *The global burden of respiratory disease—impact on child health*. Pediatric pulmonology, 2014. **49**(5): p. 430-434.
4. Thieme, S.F., S. Högl, and T.R. Johnson, *Lung ventilation*. Dual Energy CT in Clinical Practice, 2011: p. 91-99.
5. Ruppel, G.L. and P.L. Enright, *Pulmonary function testing*. Respiratory care, 2012. **57**(1): p. 165-175.
6. Haynes, J.M., D.A. Kaminsky, and G.L. Ruppel, *The Role of Pulmonary Function Testing in the Diagnosis and Management of COPD*. Respiratory Care, 2023. **68**(7): p. 889-913.
7. Powers, K.A. and A.S. Dhamoon, *Physiology, pulmonary ventilation and perfusion*. 2019.
8. Stocks, J. and A.A. Hislop, *Structure and function of the respiratory system*. Drug delivery to the lung. New York: Marcel Dekker, 2002: p. 47-104.
9. Kipritidis, J., et al., *The VAMPIRE challenge: A multi-institutional validation study of CT ventilation imaging*. Medical physics, 2019. **46**(3): p. 1198-1217.
10. Hegi-Johnson, F., et al., *Imaging of regional ventilation: Is CT ventilation imaging the answer? A systematic review of the validation data*. Radiotherapy and Oncology, 2019. **137**: p. 175-185.
11. Vinogradskiy, Y., et al., *Regional lung function profiles of stage I and III lung cancer patients: an evaluation for functional avoidance radiation therapy*. International Journal of Radiation Oncology* Biology* Physics, 2016. **95**(4): p. 1273-1280.
12. A Tahir, B., *Computed tomography ventilation imaging in lung cancer: theory, validation and application*. Detection Systems in Lung Cancer and Imaging, Volume 1, 2022: p. 8-1-8-26.
13. Horn, F.C., et al., *Regional ventilation changes in the lung: treatment response mapping by using hyperpolarized gas MR imaging as a quantitative biomarker*. Radiology, 2017. **284**(3): p. 854-861.
14. Young, R.P., R. Hopkins, and T.E. Eaton, *Forced expiratory volume in one second: not just a lung function test but a marker of premature death from all causes*. European Respiratory Journal, 2007. **30**(4): p. 616-622.
15. MacIntyre, N., *Diffusing capacity of the lung for carbon monoxide*. Respiratory Care Clinics of North America, 1997. **3**(2): p. 221-233.
16. Petousi, N., et al., *Measuring lung function in airways diseases: current and emerging techniques*. Thorax, 2019. **74**(8): p. 797-805.
17. Hughes, J., *Review series: Lung function made easy: Assessing gas exchange*. Chronic respiratory disease, 2007. **4**(4): p. 205-214.
18. Suga, K., *Technical and analytical advances in pulmonary ventilation SPECT with xenon-133 gas and Tc-99m-Technegas*. Annals of nuclear medicine, 2002. **16**: p. 303-310.
19. Siva, S., et al., *High-resolution pulmonary ventilation and perfusion PET/CT allows for functionally adapted intensity modulated radiotherapy in lung cancer*. Radiotherapy and Oncology, 2015. **115**(2): p. 157-162.
20. Townsend, D.W., et al., *PET/CT today and tomorrow*. Journal of Nuclear Medicine, 2004. **45**(1 suppl): p. 4S-14S.
21. Mariani, G., et al., *A review on the clinical uses of SPECT/CT*. European journal of nuclear medicine and molecular imaging, 2010. **37**: p. 1959-1985.
22. Kauczor, H.-U., et al., *Pulmonary ventilation imaged by magnetic resonance: at the doorstep of clinical application*. European Respiratory Journal, 2001. **17**(5): p. 1008-1023.

23. Mathew, L., et al., *Hyperpolarized 3He magnetic resonance imaging: comparison with four-dimensional x-ray computed tomography imaging in lung cancer*. Academic radiology, 2012. **19**(12): p. 1546-1553.
24. Marshall, H., et al., *In vivo methods and applications of xenon-129 magnetic resonance*. Progress in Nuclear Magnetic Resonance Spectroscopy, 2021. **122**: p. 42-62.
25. Parraga, G., et al., *Hyperpolarized 3He Magnetic Resonance Imaging of Ventilation Defects in Healthy Elderly Volunteers*. Academic Radiology, 2008. **15**(6): p. 776-785.
26. De Lange, E.E., et al., *Evaluation of Asthma With Hyperpolarized Helium-3 MRI*. Chest, 2006. **130**(4): p. 1055-1062.
27. Pinkham, D.W., et al., *A Feasibility Study of Single-inhalation, Single-energy Xenon-enhanced CT for High-resolution Imaging of Regional Lung Ventilation in Humans*. Academic radiology, 2019. **26**(1): p. 38-49.
28. Yamamoto, T., et al., *Impact of four-dimensional computed tomography pulmonary ventilation imaging-based functional avoidance for lung cancer radiotherapy*. International Journal of Radiation Oncology* Biology* Physics, 2011. **79**(1): p. 279-288.
29. Yamamoto, T., et al., *The first patient treatment of computed tomography ventilation functional image-guided radiotherapy for lung cancer*. Radiotherapy and Oncology, 2016. **118**(2): p. 227-231.
30. Jahani, N., et al., *Assessment of regional ventilation and deformation using 4D-CT imaging for healthy human lungs during tidal breathing*. Journal of Applied Physiology, 2015. **119**(10): p. 1064-1074.
31. Kipritidis, J., et al. *New pathways for end-to-end validation of CT ventilation imaging (CTVI) using deformable image registration*. in *2016 IEEE 13th International Symposium on Biomedical Imaging (ISBI)*. 2016. IEEE.
32. Yamamoto, T., et al., *Pulmonary ventilation imaging based on 4-dimensional computed tomography: comparison with pulmonary function tests and SPECT ventilation images*. International journal of radiation oncology, biology, physics, 2014. **90**(2): p. 414-422.
33. Brennan, D., et al., *Clinical validation of 4-dimensional computed tomography ventilation with pulmonary function test data*. International journal of radiation oncology, biology, physics, 2015. **92**(2): p. 423-429.
34. Woodruff, H.C., et al., *Quantifying the reproducibility of lung ventilation images between 4-Dimensional Cone Beam CT and 4-Dimensional CT*. Medical Physics, 2017. **44**(5): p. 1771-1781.
35. Kipritidis, J., et al., *Measuring interfraction and intrafraction lung function changes during radiation therapy using four-dimensional cone beam CT ventilation imaging*. Medical Physics, 2015. **42**(3): p. 1255-1267.
36. Grover, J., et al., *Investigating the use of machine learning to generate ventilation images from CT scans*. Medical Physics, 2022. **49**(8): p. 5258-5267.
37. Yamamoto, T., et al., *Four-dimensional computed tomography pulmonary ventilation images vary with deformable image registration algorithms and metrics*. Medical physics, 2011. **38**(3): p. 1348-1358.
38. Westcott, A., et al., *Chronic obstructive pulmonary disease: thoracic CT texture analysis and machine learning to predict pulmonary ventilation*. Radiology, 2019. **293**(3): p. 676-684.
39. Yang, L., et al., *Development of a radiomics nomogram based on the 2D and 3D CT features to predict the survival of non-small cell lung cancer patients*. European Radiology, 2019. **29**: p. 2196-2206.
40. Gillies, R.J., P.E. Kinahan, and H. Hricak, *Radiomics: images are more than pictures, they are data*. Radiology, 2016. **278**(2): p. 563-577.

41. Afshar, P., et al., *From handcrafted to deep-learning-based cancer radiomics: challenges and opportunities*. IEEE Signal Processing Magazine, 2019. **36**(4): p. 132-160.
42. Lafata, K.J., et al., *Radiomics: a primer on high-throughput image phenotyping*. Abdominal Radiology, 2021.
43. Liu, Z., et al., *A deep learning method for producing ventilation images from 4DCT: First comparison with technegas SPECT ventilation*. Medical Physics, 2020. **47**(3): p. 1249-1257.
44. Lafata, K.J., et al., *An exploratory radiomics approach to quantifying pulmonary function in CT images*. Scientific reports, 2019. **9**(1): p. 1-9.
45. Yang, Z., et al., *Quantification of lung function on CT images based on pulmonary radiomic filtering*. Medical Physics, 2022. **49**(11): p. 7278-7286.
46. Guidotti, R., et al., *A survey of methods for explaining black box models*. ACM computing surveys (CSUR), 2018. **51**(5): p. 1-42.
47. Fazi, M.B., *Beyond human: Deep learning, explainability and representation*. Theory, Culture & Society, 2021. **38**(7-8): p. 55-77.
48. Guerrero, T., et al., *Quantification of regional ventilation from treatment planning CT*. International Journal of Radiation Oncology* Biology* Physics, 2005. **62**(3): p. 630-634.
49. Castillo, R., et al., *Ventilation from four-dimensional computed tomography: density versus Jacobian methods*. Physics in Medicine & Biology, 2010. **55**(16): p. 4661.
50. Hegi-Johnson, F., et al., *Evaluating the accuracy of 4D-CT ventilation imaging: first comparison with Technegas SPECT ventilation*. Medical Physics, 2017. **44**(8): p. 4045-4055.
51. Wan, Y., et al., *Radiomics analysis combining unsupervised learning and handcrafted features: A multiple-disease study*. Medical Physics, 2021. **48**(11): p. 7003-7015.
52. Avanzo, M., et al., *Radiomics and deep learning in lung cancer*. Strahlentherapie und Onkologie, 2020. **196**: p. 879-887.
53. Xu, Y., et al., *Deep learning predicts lung cancer treatment response from serial medical imaging*. Clinical Cancer Research, 2019. **25**(11): p. 3266-3275.
54. Zhong, Y., et al., *Deriving ventilation imaging from 4 DCT by deep convolutional neural network*. Medical physics, 2019. **46**(5): p. 2323-2329.
55. Yang, Z., et al., *Development of a multi-feature-combined model: proof-of-concept with application to local failure prediction of post-SBRT or surgery early-stage NSCLC patients*. Frontiers in Oncology, 2023. **13**.
56. Siddique, N., et al., *U-net and its variants for medical image segmentation: A review of theory and applications*. Ieee Access, 2021. **9**: p. 82031-82057.
57. Kajikawa, T., et al., *A deep learning method for translating 3DCT to SPECT ventilation imaging: First comparison with 81mKr-gas SPECT ventilation imaging*. Medical Physics, 2022. **49**(7): p. 4353-4364.
58. Petch, J., S. Di, and W. Nelson, *Opening the black box: the promise and limitations of explainable machine learning in cardiology*. Canadian Journal of Cardiology, 2022. **38**(2): p. 204-213.
59. Esling, P. and C. Agon, *Time-series data mining*. ACM Computing Surveys (CSUR), 2012. **45**(1): p. 1-34.
60. Fu, T.-c., *A review on time series data mining*. Engineering Applications of Artificial Intelligence, 2011. **24**(1): p. 164-181.
61. Newbold, P. and C.W. Granger, *Experience with forecasting univariate time series and the combination of forecasts*. Journal of the Royal Statistical Society: Series A (General), 1974. **137**(2): p. 131-146.
62. Wei, W.W., *Multivariate time series analysis and applications*. 2019: John Wiley & Sons.

63. Fulcher, B.D., *Feature-based time-series analysis*, in *Feature engineering for machine learning and data analytics*. 2018, CRC press. p. 87-116.
64. Yu, Y., et al., *A review of recurrent neural networks: LSTM cells and network architectures*. *Neural computation*, 2019. **31**(7): p. 1235-1270.
65. Elman, J.L., *Finding structure in time*. *Cognitive science*, 1990. **14**(2): p. 179-211.
66. Jordan, M.I., *Attractor dynamics and parallelism in a connectionist sequential machine*, in *Artificial neural networks: concept learning*. 1990. p. 112-127.
67. Chen, T.-B. and V.-W. So. *A comparative study of recurrent neural network architectures on learning temporal sequences*. in *Proceedings of International Conference on Neural Networks (ICNN'96)*. 1996. IEEE.
68. Šter, B., *Selective recurrent neural network*. *Neural processing letters*, 2013. **38**: p. 1-15.
69. Smagulova, K. and A.P. James, *A survey on LSTM memristive neural network architectures and applications*. *The European Physical Journal Special Topics*, 2019. **228**(10): p. 2313-2324.
70. Lipton, Z.C., J. Berkowitz, and C. Elkan, *A critical review of recurrent neural networks for sequence learning*. arXiv preprint arXiv:1506.00019, 2015.
71. Hochreiter, S. and J. Schmidhuber, *Long short-term memory*. *Neural computation*, 1997. **9**(8): p. 1735-1780.
72. Graves, A. and J. Schmidhuber, *Framewise phoneme classification with bidirectional LSTM and other neural network architectures*. *Neural networks*, 2005. **18**(5-6): p. 602-610.
73. Graves, A. and J. Schmidhuber. *Framewise phoneme classification with bidirectional LSTM networks*. in *Proceedings. 2005 IEEE International Joint Conference on Neural Networks, 2005*. 2005. IEEE.
74. Vaswani, A., *Attention is all you need*. arXiv preprint arXiv:1706.03762, 2017.
75. Qi, Z., S. Khorram, and F. Li. *Visualizing Deep Networks by Optimizing with Integrated Gradients*. in *CVPR workshops*. 2019.
76. Simonyan, K., *Deep inside convolutional networks: Visualising image classification models and saliency maps*. arXiv preprint arXiv:1312.6034, 2013.
77. Smilkov, D., et al., *Smoothgrad: removing noise by adding noise*. arXiv preprint arXiv:1706.03825, 2017.
78. Tjoa, E. and C. Guan, *Quantifying explainability of saliency methods in deep neural networks*. arXiv preprint arXiv:2009.02899, 2020.
79. Gomez, T. and H. Mouchère, *Computing and evaluating saliency maps for image classification: a tutorial*. *Journal of Electronic Imaging*, 2023. **32**(2): p. 020801-020801.
80. Muhammad, D. and M. Bendeche, *Unveiling the black box: A systematic review of Explainable Artificial Intelligence in medical image analysis*. *Computational and structural biotechnology journal*, 2024.
81. Chaddad, A., et al., *Survey of explainable AI techniques in healthcare*. *Sensors*, 2023. **23**(2): p. 634.
82. Singh, A., S. Sengupta, and V. Lakshminarayanan, *Explainable deep learning models in medical image analysis*. *Journal of imaging*, 2020. **6**(6): p. 52.
83. Ismail, A.A., et al., *Benchmarking deep learning interpretability in time series predictions*. *Advances in neural information processing systems*, 2020. **33**: p. 6441-6452.
84. Wang, Y., et al., *Gradient based Feature Attribution in Explainable AI: A Technical Review*. arXiv preprint arXiv:2403.10415, 2024.
85. Wang, C., et al., *Assessment of concurrent stereotactic radiosurgery and bevacizumab treatment of recurrent malignant gliomas using multi-modality MRI imaging and radiomics analysis*. *Journal of Radiosurgery and SBRT*, 2018. **5**(3): p. 171.

86. Yu, H., et al., *Texture analysis as a radiomic marker for differentiating renal tumors*. *Abdominal Radiology*, 2017. **42**: p. 2470-2478.
87. Haralick, R.M., K. Shanmugam, and I.H. Dinstein, *Textural features for image classification*. *IEEE Transactions on systems, man, and cybernetics*, 1973(6): p. 610-621.
88. Tang, X., *Texture information in run-length matrices*. *IEEE Transactions on Image Processing*, 1998. **7**(11): p. 1602-1609.
89. Berenguer, R., et al., *Radiomics of CT features may be nonreproducible and redundant: influence of CT acquisition parameters*. *Radiology*, 2018. **288**(2): p. 407-415.
90. Wu, Y., et al., *Grading glioma by radiomics with feature selection based on mutual information*. *Journal of Ambient Intelligence and Humanized Computing*, 2018. **9**: p. 1671-1682.
91. Sedgwick, P., *Pearson's correlation coefficient*. *Bmj*, 2012. **345**.
92. Zhao, Y., G. Karypis, and U. Fayyad, *Hierarchical clustering algorithms for document datasets*. *Data mining and knowledge discovery*, 2005. **10**: p. 141-168.
93. Myers, L. and M.J. Sirois, *Spearman correlation coefficients, differences between*. *Encyclopedia of statistical sciences*, 2004. **12**.
94. Peng, T., et al., *An integrated framework of Bi-directional long-short term memory (BiLSTM) based on sine cosine algorithm for hourly solar radiation forecasting*. *Energy*, 2021. **221**: p. 119887.
95. Yu, L., et al., *A novel hierarchical algorithm for bearing fault diagnosis based on stacked LSTM*. *Shock and Vibration*, 2019. **2019**.
96. Krause, B., et al., *Multiplicative LSTM for sequence modelling*. arXiv preprint arXiv:1609.07959, 2016.
97. Memory, L.S.-T., *Long short-term memory*. *Neural computation*, 2010. **9**(8): p. 1735-1780.
98. Sundararajan, M., A. Taly, and Q. Yan. *Axiomatic attribution for deep networks*. in *International conference on machine learning*. 2017. PMLR.
99. Kipritidis, J., *TU-H-202-04: The VAMPIRE Challenge: Preliminary Results From a Multi-Institutional Study of CT Ventilation Image Accuracy*. *Medical physics*, 2016. **43**(6Part36): p. 3771-3771.
100. Zhang, Y., Q. Liu, and L. Song, *Sentence-state LSTM for text representation*. arXiv preprint arXiv:1805.02474, 2018.
101. Takase, S. and N. Okazaki, *Positional encoding to control output sequence length*. arXiv preprint arXiv:1904.07418, 2019.
102. Diakogiannis, F.I., et al., *ResUNet-a: A deep learning framework for semantic segmentation of remotely sensed data*. *ISPRS Journal of Photogrammetry and Remote Sensing*, 2020. **162**: p. 94-114.
103. Zhou, Z., et al., *Unet++: Redesigning skip connections to exploit multiscale features in image segmentation*. *IEEE transactions on medical imaging*, 2019. **39**(6): p. 1856-1867.
104. Raza, R., et al., *dResU-Net: 3D deep residual U-Net based brain tumor segmentation from multimodal MRI*. *Biomedical Signal Processing and Control*, 2023. **79**: p. 103861.
105. Jensen, L.J., et al., *Stability of Liver Radiomics across Different 3D ROI Sizes—An MRI In Vivo Study*. *Tomography*, 2021. **7**(4): p. 866-876.
106. Lafata, K., et al., *Spatial-temporal variability of radiomic features and its effect on the classification of lung cancer histology*. *Physics in Medicine & Biology*, 2018. **63**(22): p. 225003.
107. Aerts, H.J.W.L., et al., *Decoding tumour phenotype by noninvasive imaging using a quantitative radiomics approach*. *Nature Communications*, 2014. **5**(1).
108. Guo, W., et al., *Prediction of clinical phenotypes in invasive breast carcinomas from the integration of radiomics and genomics data*. *Journal of medical imaging*, 2015. **2**(4): p. 041007.

109. Zwanenburg, A., et al., *The Image Biomarker Standardization Initiative: Standardized Quantitative Radiomics for High-Throughput Image-based Phenotyping*. Radiology, 2020. **295**(2): p. 328-338.
110. Chang, Y., et al., *Digital phantoms for characterizing inconsistencies among radiomics extraction toolboxes*. Biomedical Physics & Engineering Express, 2020.
111. Höllig, J., C. Kulbach, and S. Thoma, *TSInterpret: A Python Package for the Interpretability of Time Series Classification*. Journal of Open Source Software, 2023. **8**(85): p. 5220.
112. Carvalho, P.R., C.S. Munita, and A.L. Lapolli, *Validity studies among hierarchical methods of cluster analysis using cophenetic correlation coefficient*. Brazilian Journal of Radiation Sciences, 2019. **7**(2A (Suppl.)).
113. Dinh, D.-T., T. Fujinami, and V.-N. Huynh. *Estimating the optimal number of clusters in categorical data clustering by silhouette coefficient*. in *Knowledge and Systems Sciences: 20th International Symposium, KSS 2019, Da Nang, Vietnam, November 29–December 1, 2019, Proceedings 20*. 2019. Springer.
114. Dalmaijer, E.S., C.L. Nord, and D.E. Astle, *Statistical power for cluster analysis*. BMC bioinformatics, 2022. **23**(1): p. 205.
115. Nayak, K.S., et al., *Real-time magnetic resonance imaging*. Journal of Magnetic Resonance Imaging, 2022. **55**(1): p. 81-99.
116. Freislederer, P., et al., *Recent advances in surface guided radiation therapy*. Radiation Oncology, 2020. **15**: p. 1-11.
117. Chen, L., et al., *Accuracy of real-time respiratory motion tracking and time delay of gating radiotherapy based on optical surface imaging technique*. Radiation Oncology, 2020. **15**: p. 1-9.
118. Zhou, Z., et al., *Models genesis*. Medical image analysis, 2021. **67**: p. 101840.
119. Wei, S., et al., *Multi-temporal SAR data large-scale crop mapping based on U-Net model*. Remote Sensing, 2019. **11**(1): p. 68.
120. Ali, J., et al., *Random forests and decision trees*. International Journal of Computer Science Issues (IJCSI), 2012. **9**(5): p. 272.
121. Van Griethuysen, J.J., et al., *Computational radiomics system to decode the radiographic phenotype*. Cancer research, 2017. **77**(21): p. e104-e107.
122. Mo, X., et al., *Abnormal pulmonary function in COVID-19 patients at time of hospital discharge*. European Respiratory Journal, 2020. **55**(6).
123. Ngai, J.C., et al., *The long-term impact of severe acute respiratory syndrome on pulmonary function, exercise capacity and health status*. Respirology, 2010. **15**(3): p. 543-550.
124. Hui, D.S., et al., *The 1-year impact of severe acute respiratory syndrome on pulmonary function, exercise capacity, and quality of life in a cohort of survivors*. Chest, 2005. **128**(4): p. 2247-2261.
125. Guerrero, T., et al., *Dynamic ventilation imaging from four-dimensional computed tomography*. Physics in Medicine & Biology, 2006. **51**(4): p. 777.
126. Simon, B.A., *Non-invasive imaging of regional lung function using x-ray computed tomography*. Journal of clinical monitoring and computing, 2000. **16**(5): p. 433-442.
127. Kunitatsu, A., et al., *Comparison between glioblastoma and primary central nervous system lymphoma using MR image-based texture analysis*. Magnetic Resonance in Medical Sciences, 2018. **17**(1): p. 50-57.
128. Gillis, H.L. and K.R. Lutchen, *How heterogeneous bronchoconstriction affects ventilation distribution in human lungs: a morphometric model*. Annals of biomedical engineering, 1999. **27**: p. 14-22.

129. Emami, K., et al., *Regional correlation of emphysematous changes in lung function and structure: a comparison between pulmonary function testing and hyperpolarized MRI metrics*. Journal of applied physiology, 2011. **110**(1): p. 225-235.
130. Xue, P., et al., *Effective lung ventilation estimation based on 4D CT image registration and supervoxels*. Biomedical Signal Processing and Control, 2023. **79**: p. 104074.
131. Jahani, N., et al., *A four-dimensional computed tomography comparison of healthy and asthmatic human lungs*. Journal of biomechanics, 2017. **56**: p. 102-110.
132. Ueha, R., et al., *Sleep-induced glottis closure in multiple system atrophy evaluated by four-dimensional computed tomography*. Frontiers in Medicine, 2020. **7**: p. 132.
133. Hu, W.-T., et al., *Quantitative analyzes of the variability in airways via four-dimensional dynamic ventilation CT in patients with chronic obstructive pulmonary disease: correlation with spirometry data and severity of airflow limitation*. Journal of Thoracic Disease, 2023. **15**(9): p. 4775.
134. Yaremko, B.P., et al., *Reduction of normal lung irradiation in locally advanced non-small-cell lung cancer patients, using ventilation images for functional avoidance*. International Journal of Radiation Oncology* Biology* Physics, 2007. **68**(2): p. 562-571.
135. Dombret, M.-C., et al., *Bronchial thermoplasty: a new therapeutic option for the treatment of severe, uncontrolled asthma in adults*. European Respiratory Review, 2014. **23**(134): p. 510-518.
136. Gesierich, W., et al., *Collapse phenomenon during Chartis collateral ventilation assessment*. European Respiratory Journal, 2016. **47**(6): p. 1657-1667.
137. Davey, C., et al., *Bronchoscopic lung volume reduction with endobronchial valves for patients with heterogeneous emphysema and intact interlobar fissures (the BeLieVeR-HIFi study): a randomised controlled trial*. The Lancet, 2015. **386**(9998): p. 1066-1073.